

A detailed input-output characterization of single neurons reveals the synaptic basis of spontaneous spiking in recurrent networks

Julian Bartram^{1,†}, Felix Franke², Sreedhar Saseendran Kumar¹, Alessio Paolo Buccino¹, Xiaohan Xue¹, Tobias Gänswain¹, Manuel Schröter¹, Taehoon Kim¹, Krishna Chaitanya Kasuba¹, and Andreas Hierlemann¹

¹ETH Zurich, Department of Biosystems Science and Engineering, Basel, Switzerland.

²Institute of Molecular and Clinical Ophthalmology Basel, Basel, Switzerland

† correspondence: julian.bartram@bsse.ethz.ch

Abstract

Self-sustained recurrent activity in cortical networks is thought to be important for multiple crucial processes, including circuit development and homeostasis. However, the precise relationship between synaptic input patterns and spiking output of individual neurons remains unresolved during spontaneous network activity. Here, using whole-network high-density microelectrode array (HD-MEA) recordings and patch clamping, we developed a novel experimental approach and analytical tools that provide a comprehensive long-term input-output characterization of individual neurons in cortical cell cultures. We found that, during in vivo-like network activity with excitation(E)-inhibition(I) balance, postsynaptic spiking coincided with the maxima of rapid, network state-dependent fluctuations in the input E/I ratio. Our approach also uncovered the underlying circuit architecture and we identified a few key inhibitory inputs – often from special hub neurons – that were instrumental in mediating these E/I ratio changes. Balanced network theory predicts dynamical regimes governed by input fluctuation and featuring a fast neuronal responsiveness. Our findings – obtained in self-organized neuronal cultures – suggest that the emergence of these favorable regimes and associated network architectures is an inherent property of all cortical networks.

Introduction

Neurons typically receive a continuous bombardment by orchestrated excitatory and inhibitory synaptic inputs, which ultimately determines postsynaptic spiking. Such a continuous input activation is a basic operational principle of cortical networks that has been observed in awake animals¹⁻³, up states recorded during slow-wave sleep^{1,4} and in brain slices⁵⁻⁷, and periods of heightened network activity in cell cultures⁸⁻¹¹. The observed input barrages can be generated – to a large extent or completely in the in vitro cases – by

spontaneous recurrent network activity. Self-maintained recurrent activity is the basis for numerous important processes such as synaptic homeostasis¹², a mediation of circuit refinements¹³ and working memory¹⁴, but the network properties and dynamics that give rise to and shape spontaneous activity are poorly understood.

It has previously been shown that the excitatory (E) and inhibitory (I) inputs received by individual neurons are approximately balanced through local circuit interactions during both evoked and spontaneous network activity^{6-8,15}. The approximate input balance raises the question of precisely which synaptic activation patterns are actually associated with postsynaptic spiking. The answer to this question could provide insights into the dynamical regime in which networks operate and has, therefore, important implications for network function¹⁶. Theoretical work suggests that balanced networks can potentially assume multiple different dynamical states¹⁷. When global spiking is asynchronous and neuronal firing is irregular – as often observed in cortical networks during wakefulness – neural networks may operate in a so-called fluctuation-driven regime. In this dynamical state, the mean neuronal membrane potential is just below the action potential threshold, and fast input fluctuations trigger postsynaptic spiking (i.e., due to an increase in excitation or decrease in inhibition)¹⁶⁻¹⁹. In another regime, synaptic inputs are more synchronized, and the synchronization of especially inhibitory synaptic inputs can generate effective membrane potential fluctuations^{20,21}. This synchronized activity can be organized by fast rhythms, such as gamma oscillations^{21,22}. The described asynchronous and synchronous regimes, with a mean membrane potential just below threshold, have favorable properties: Neurons can respond rapidly to small input changes, and multiple different combinations of E-I conductance changes can control spiking. However, theoretical work also predicts the existence of other dynamical regimes. For instance, the neuronal output could be governed by mean-driven spiking, which is characterized by supra-threshold mean membrane potentials^{23,24}. In this case, a precise spike timing cannot be readily achieved by fast and small input changes.

To better understand and characterize the dynamical regimes that are actually implemented in biological neural networks, our goal was to experimentally identify the synaptic events that determine postsynaptic spiking during spontaneous network activity. For such an investigation, information on *i*) excitatory and *ii*) inhibitory synaptic input activity in conjunction with *iii*) postsynaptic spike times is needed. However, with existing techniques, it is impractical to perform these three measurements in parallel. Through single-channel patch clamping, for example, one can only isolate either excitatory or inhibitory input currents or postsynaptic spike times. Approaches involving dual-patch clamping of adjacent cells – to simultaneously acquire different modalities – rely on strongly correlated activity between the target cells^{25,26}. This issue is further exacerbated when three simultaneous measurements are needed, as in our investigation. Alternatively, the dynamic clamp technique and computational modelling^{21,27} may be used to investigate the modulation of spike timing by artificial synaptic conductances. However, these approaches are limited in their ability to

recapitulate the full complexity of the activity generated by biological neural networks.

To address the existing methodological shortcomings, we developed a novel experimental approach and analytical tools that provide – in parallel – a reconstruction of the excitatory and inhibitory synaptic input activity during a period of recorded postsynaptic spiking (**Fig. 1a**). The result of this reconstruction is a detailed input-output characterization of individual neurons over multiple hours. We used cortical cell cultures that produced E-I balanced spontaneous recurrent network activity with similarities to cortical up-down state oscillations of deep sleep^{7,8,28}. This in vitro model was, by nature, free of external inputs, permitted control over the network size, and, crucially, allowed for recording of spiking activity from virtually every neuron in the network. Our method combines high-density microelectrode array (HD-MEA) recordings with patch clamping and includes a comprehensive identification of incoming monosynaptic connections. Far exceeding state-of-the-art methods, we identified up to 20 spontaneously active incoming monosynaptic connections to a single postsynaptic cell and determined the corresponding evoked postsynaptic currents.

We used the developed approach to examine the synaptic events that determine spontaneous spiking in excitatory cells. We observed rapid, network-state dependent escalations of the synaptic input E/I ratio with durations down to only a few milliseconds. Postsynaptic spikes were typically triggered precisely at the maxima of these transient surges of the E/I ratio, indicating a sophisticated network organization. The relative synaptic contributions to these E/I fluctuations were postsynaptic cell-dependent. Our method also revealed the circuit architecture that mediated the observed spiking regime. We found that individual neurons were strongly regulated by a few key inhibitory inputs. These inputs were often provided by special hub neurons featuring strong synapses, high spike rates and fast spike propagation speeds. Our findings – in line with theoretical predictions for cortical networks in vivo – suggest that it is an inherent property of cortical networks in general to self-organize towards sophisticated circuit architectures that give rise to favorable dynamical regimes.

Results

Reconstructing synaptic input activity during postsynaptic spiking

The key steps to reconstruct the excitatory and inhibitory synaptic input currents of an individual postsynaptic neuron, during a period of recorded postsynaptic spiking, are as follows (**Fig. 1a**): *i*) Acquire long-term whole-network extracellular recordings of spontaneous neuronal spiking. *ii*) Identify the incoming monosynaptic connections onto individual postsynaptic cells, and calculate the mean evoked postsynaptic currents for each connection. *iii*) Identify the postsynaptic and presynaptic neurons in the long-term extracellular

recording period to obtain parallel spike trains. With the spike trains of the presynaptic cells and the corresponding estimates of the evoked currents, reconstruct the excitatory and inhibitory synaptic input currents experienced by the target cell during postsynaptic spiking. In the first part of this study, we will elaborate on how each of these steps was implemented.

Our experimental pipeline is depicted in **Fig. 1b-f**. Primary rat cortical neurons were plated on a HD-MEA chip featuring 26'400 electrodes and 1024 channels for simultaneous readout (**Fig. 1b**). Following network maturation, brief sequential recordings – covering together the entire HD-MEA chip – were performed to identify electrodes that detected neuronal activity. Active electrodes were subsequently selected for long-term recording of network-wide spiking. Extracellular data were acquired for at least 3 h (**Fig. 1c**) and spike sorted to identify individual units (**Fig. 1d**). Next, selected cells were patched, and paired HD-MEA and patch-clamp recordings were obtained (**Fig. 1e**). Postsynaptic spikes were recorded in whole-cell current-clamp or cell-attached mode, and using these spike times to generate the spike-triggered average of each HD-MEA electrode trace revealed the extracellular signature of the patched cell (here referred to as the cell or unit ‘footprint’). This footprint was matched to a unit footprint from the spike-sorted long-term recording that preceded the patch-clamp experiment in order to obtain the long-term spike train of the patched cell.

In the final experimental step, we performed a second paired HD-MEA and patch-clamp recording to measure excitatory postsynaptic currents (EPSCs) in whole-cell voltage-clamp mode in addition to recording simultaneously extracellular network spiking (**Fig. 1f**). We used this second paired recording to estimate the average EPSC that was evoked in the patched cell by each of the extracellularly recorded neurons in the network – which enabled us to identify the neurons that were presynaptic to the patched cell. Note that a high-chloride internal patch-clamp solution was used and this shifted the chloride reversal potential. As a consequence of this shift, one voltage-clamp recordings at -70 mV holding potential was sufficient to simultaneously measure postsynaptic currents that were evoked by both glutamatergic (excitatory) and GABAergic (typically inhibitory) connections. Under such conditions, GABAergic presynaptic cells also evoke net-inward currents (i.e., EPSCs) in the patched cell. We will later introduce a procedure to classify the connection type.

Connectivity inference and EPSC estimation based on paired HD-MEA and patch-clamp recordings

We used the paired HD-MEA and whole-cell patch-clamp recordings from individual postsynaptic cells to identify all presynaptically connected neurons and to obtain an EPSC estimate for each incoming connection. Our method assumes that the patch-clamp current trace I at time point t is a linear superposition of the

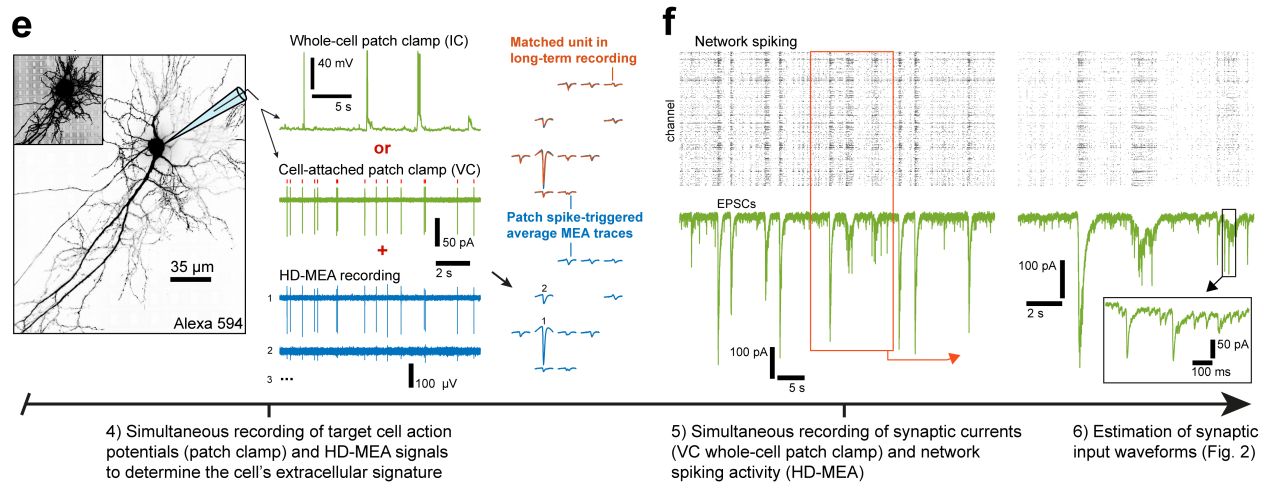
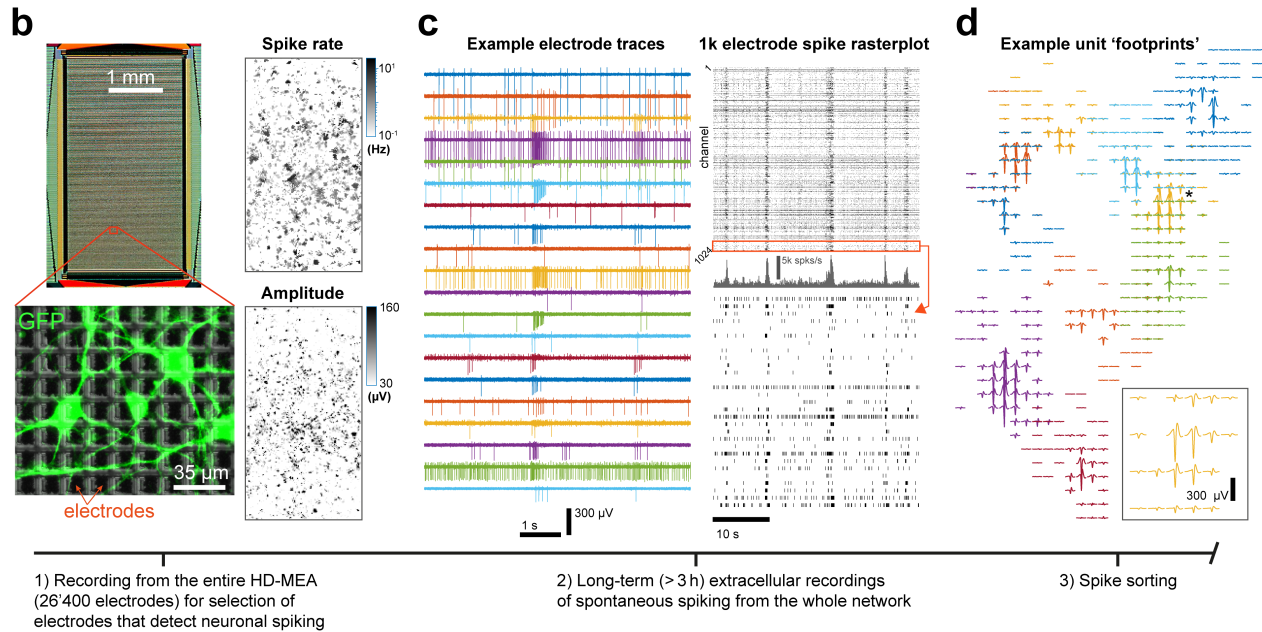
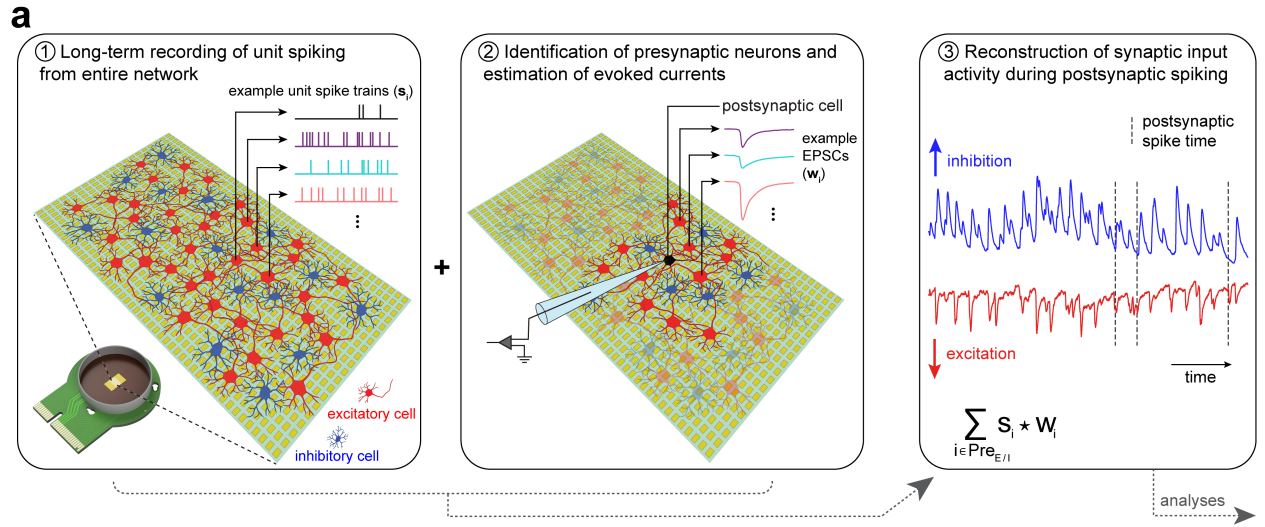


Figure 1. Concept and experimental approach for reconstructing synaptic input activity during postsynaptic spiking

(a) Schematic of main concept. Whole-network extracellular recordings are performed, followed by connectivity inference based on simultaneous HD-MEA and patch-clamp recordings. Subsequently, spike trains (s_i) of all identified excitatory (Pre_E) or inhibitory (Pre_I) presynaptic cells are convolved with their respective postsynaptic-current estimate to obtain, for several hours, reconstructions of synaptic input activity. Crucially, postsynaptic spike times are also available during the reconstruction period. The experimental implementation of this approach is shown in (b-f).

Main analytical steps are introduced in Figures 2 and 3.

(b) Left: Sensing area of a HD-MEA chip and magnified region with cultured primary neurons. The magnified image is a confocal fluorescence/bright-field composite and illustrates the relative size of cells and electrodes (distance between adjacent electrodes: $17.5 \mu\text{m}$). Right: whole-array spike rate and amplitude maps. Electrodes displaying spiking activity were selected for subsequent long-term recording steps (grouped in 2-3 subsets of 1024 electrodes each).

(c) Left: example electrode traces of a long-term recording. Right: spike raster plot of one entire electrode subset. These recordings revealed a rich repertoire of cell-spiking behaviors and complex network dynamics alternating between high- and low-activity periods. Experiments were performed between days in vitro 15-18. The total recording time for each electrode was at least 3 h.

(d) Example spike-triggered average extracellular unit ‘footprints’ (i.e., the extracellular electrical-potential distribution of the respective neuron across all selected array electrodes), following spike sorting. A black asterisk marks the footprint magnified in the inset. Trace ‘gaps’ indicate electrodes that did not exhibit neuronal activity in (b) and were hence not selected for long-term recording. Typically 100–200 units were identified per subset of 1024 electrodes.

(e) Left: fluorescence image of a patched cell (inverted), with the inset showing the same cell, following intensity adjustments, to visualize the HD-MEA electrodes underneath. Middle: example traces from a simultaneous patch-clamp (green; either in current clamp [IC] or voltage clamp [VC] mode) and HD-MEA (blue) recording. Right: spike-triggered averaging of the extracellular signals, based on spike times detected via the patch-clamp electrode, revealed the HD-MEA footprint of the patched cell (blue traces; only the electrodes traces with a significant negative peak shown here). The footprint of the patched cell was matched to a unit footprint from the preceding spike-sorted long-term recording (orange).

(f) Electrode spike raster plot (top) and voltage-clamp trace (green; bottom) of a simultaneous HD-MEA and whole-cell patch-clamp recording. With this second paired recording, presynaptic cells that formed monosynaptic connections with the patched cell were identified, and the corresponding EPSC waveforms were estimated (see Fig. 2).

In all panels, HD-MEA electrode traces were band-pass filtered at 0.3–9.5 kHz.

EPSCs of all neurons in the network:

$$I(t) = \sum_{i=1}^{N_c} \sum_{\tau=0}^{N_\tau} s_i(t - \tau) w_i(\tau), \quad (1)$$

where w_i is the EPSC waveform estimate (or, simply, EPSC) for the i^{th} neuron in the network, and $s_i(t)$ represents the corresponding (binary) spike train that indicates if neuron i spiked at time point t . N_τ is the number of sample time points of the EPSC estimates. N_c is the number of neurons in the network, which is the number of units resulting from spike sorting the HD-MEA data of the respective paired recording. Since we measured both the current trace (I) and the spike trains of the units in the network (s_i), we can obtain the EPSC waveform estimates (w_i) by linear regression. We adapted a previously published solution²⁹ to this regression problem (see Methods for details), and upon its application to our paired recording data, a large number of synaptic EPSCs with a characteristic fast rising phase and a slow decay was identified (**Fig. 2**). In **Fig. 2a**, the monosynaptic connections and w_i estimates are shown for one representative postsynaptic neuron. This example postsynaptic cell had 13 incoming connections with varying synaptic strengths and response onset latencies, while the > 100 remaining neurons/units in the network were putatively unconnected, as evident by their relatively flat EPSC estimate (i.e., these neurons did not show a significant evoked current).

To assess the EPSC estimation results, we performed reconstructions of the patch-clamp current trace based on the EPSC estimates and corresponding spike trains. The reconstruction was achieved by applying the right term of equation (1). Two different reconstructions were generated for each of the patched cells (**Fig. 2b**, same example cell as in Fig. 2a). For the first reconstruction (magenta), we used the w_i and s_i of all neurons/units in the network. For the second reconstruction (green), we only included the presynaptic cells forming a putative connection with the patched neuron. Note the often remarkable matching of measured (black) and reconstructed current traces. The two current-trace reconstructions were often very similar, indicating that the identified monosynaptic connections accounted for most of the observed currents. Some deviations were observed during periods of heightened activity, where especially slow currents played a role (e.g., see bottom-right traces in **Fig. 2b**). One possibility is that some of the non-EPSC-like waveforms accounted for other small evoked currents, such as currents associated with an activation of extra-synaptic receptors.

Our regression approach was robust and reliably produced EPSC estimates under varying network-activity levels (**Fig. 2c**). Across a total of 14 patched putatively excitatory cells, 142 incoming connections were identified (mean = 10.1 ± 5.2 SD; min = 3, max = 20 connections per cell). Excellent reconstruction performance was achieved across experiments (median variance explained = 0.65; **Fig. 2d**) – especially as some deviation were to be expected, e.g., due to transmission failures in the measured trace. Finally, we validated our regression approach by simulation of ground-truth synaptic inputs (**Fig. 2e**; see Methods for details). The simulation results suggested that our approach would only have failed to identify connections with extremely small-amplitude EPSCs and very low presynaptic spike rates.

In **Fig. 1e**, we described how the unit that corresponds to the patched cell can be identified in the long-term recording of network spiking that preceded the patch-clamp experiments by footprint matching. In a similar manner, we obtained parallel long-term spike trains of the presynaptic neurons that were identified by our regression method.

Connection-type classification based on network-wide spike transmission or suppression

The usage of a high-chloride internal patch-clamp solution meant that both glutamatergic and GABAergic presynaptic cells evoked EPSCs in the patched cell, and, hence, a way to distinguish between the connection types was required. Here, we performed a connection-type classification by directly assessing if the respective presynaptic neuron had an inhibitory (i.e., suppressing) or excitatory (i.e., facilitating) effect on network-wide neuronal spiking. Using the > 3 h spike trains that were available for the presynaptic neurons, we computed

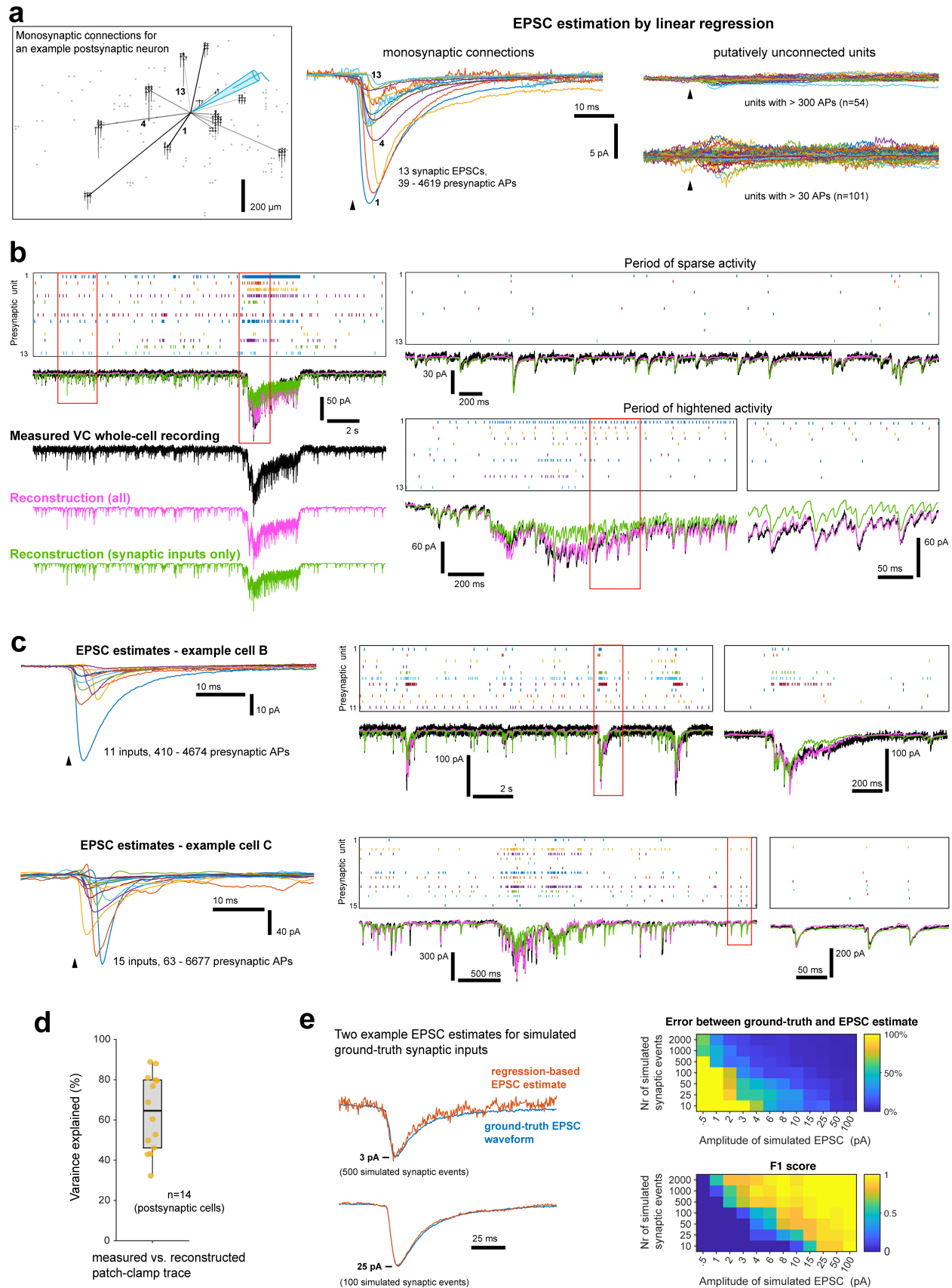


Figure 2

Figure 2. Connectivity inference and EPSC estimation based on paired HD-MEA and patch-clamp recordings

(a) Results from one example paired HD-MEA and VC whole-cell patch-clamp recording. Our regression method estimates the EPSC waveform for each unit in the network. Middle: EPSCs of putative connections (amplitude $> 10 \times$ standard deviation of pre-spike baseline & amplitude > 1 pA). Black arrowhead indicates presynaptic spike time. Right: EPSC estimates of putatively unconnected units. Left: spatial distribution of the presynaptic and postsynaptic cells (footprints of presynaptic units plotted in black; connection lines indicate synaptic strengths: the more transparent the the weaker the connection). Locations of unconnected units are indicated by grey dots.

(b) For the same paired recording as in (a), example recording period with a raster plot of presynaptic unit spiking (top), the VC patch-clamp recording (black), and two current-trace reconstructions using unit spike times and EPSC estimates of either all units (magenta) or only the putatively connected units (green).

(c) EPSC estimates and current-trace reconstructions for two more example paired recordings with varying activity levels.

(d) Variance of the measured patch-clamp recording explained by the respective current-trace reconstruction with all units (14 patched cells, with 142 identified connections, from 5 preparations). Box plot indicates median and interquartile ranges, and whiskers the minimum/maximum values.

(e) Validation of the regression-approach by simulation of ground-truth synaptic inputs. Ground-truth EPSC waveforms were added to the 14 patch-clamp current traces, followed by EPSC estimation using the regression approach. Left: comparison of two example EPSC estimates with the corresponding ground-truth EPSC. Right: mean errors between ground-truth and EPSC estimate (top) and F1 score (bottom) for different simulation parameter combinations ($n = 14$ simulations each). The F1 score is a performance metric that combines recall and precision (see Methods for details).

See also Supplementary Fig. 1 for evidence that the variation in the number of identified inputs is of biological origin.

the pairwise cross-correlograms (CCGs) and subsequently extracted the spike-transmission probability (STP) from each CCG (**Fig. 3a**; see Methods for details). The resulting STP measure is expected to be positive for excitatory connections and negative for inhibitory connections³⁰. For cell-type classification, we computed a STP matrix based on all pre- and postsynaptic units that were recorded in parallel (**Fig. 3b**). A unit was then classified as putatively excitatory or inhibitory, if the mean (outgoing) STP value was positive or negative, respectively.

For 10 out of a total of 15 patched cells, the postsynaptic unit could be identified in the long-term HD-MEA recordings (see **Fig. 1e**); For the remaining 5, there was either no unit template available, or there was no matching unit found. Consistent with our attempt to target pyramidal cells, 9 out of the 10 cells with postsynaptic unit were classified as excitatory (mean STP > 0 ; mean spike rate = $1.2 \text{ Hz} \pm 0.5 \text{ Hz SD}$) and only 1 cell was classified as inhibitory (mean STP < 0 ; spike rate = 9.6 Hz ; cell subsequently excluded).

Following the cell-type classification, EPSC estimates could be attributed to an excitatory ('excEPSC') or inhibitory ('inhEPSC') connection. In line with known synaptic properties³¹, the mean excEPSC across experiments exhibited faster kinetics compared to the mean inhEPSC (**Fig. 3c**). In this work, the term 'EPSC' refers to both excEPSCs and inhEPSCs. For a better comparison of excitatory and inhibitory synaptic activity, we also converted currents to conductances – separately for excEPSCs and inhEPSCs – based on the respective driving forces for glutamatergic and GABAergic ion channels. Note that this conversion expresses the effective conductance at the soma (the location of the patch-clamp electrode). In the following sections, we used the conductances for direct comparisons between excitatory and inhibitory inputs, and, otherwise, the exc/inhEPSC amplitudes.

Further supporting the validity of the classification approach, we also found striking differences in the extracellular footprint characteristics of the presynaptic neurons classified as excitatory and inhibitory, re-

spectively (**Supplementary Fig. 2**). Inhibitory cells exhibited a faster action potential propagation and larger footprint size, while excitatory cells had a more distant axonal projection. These footprint results were in agreement with fluorescence images of putative inhibitory and excitatory cells (**Fig. 3d**). The E/I classification concludes the main methodological part of this study.

Relationship between connection strength and STP at single postsynaptic-cell level indicates crucial role for few strong connections in spike timing

After performing the analytical steps, detailed in the previous sections, we had identified multiple excitatory and inhibitory monosynaptic connections onto individual postsynaptic cells with corresponding estimates of the evoked postsynaptic currents. Moreover, long-term parallel spike trains of presynaptic and postsynaptic spiking activity were available (see **Fig. 1a**). We exploited these data sets to investigate how synaptic activity relates to postsynaptic spiking. First, we focused on the role of individual monosynaptic connections, and, in particular, we examined the relationship between connection strength (i.e., EPSC amplitude) and the STP of the respective connection (**Fig. 4**).

While STP has been suggested as a proxy for synaptic strength^{32,33}, supporting experimental data is actually scarce. In fact, the influence of an individual connection on postsynaptic spiking is, besides connection strength, also strongly determined by the correlation of its activity with the activation of the other incoming connections. Varying input correlations and also variations in intrinsic neuronal properties could cause differences in the connection strength-STP relationship across different postsynaptic cells. To gain a clearer picture of the spike-facilitating or spike-suppressive effects of monosynaptic connections at postsynaptic-cell level, we calculated pairwise spike-time cross-correlations based on the spike trains of the presynaptic and postsynaptic neurons. As the time delay between presynaptic spike and postsynaptic exc/inhEPSC onset was known for each connection, we could align the STP quantification window to the response onset and, in this way, extract a further optimized STP estimate (**Fig. 4a**). For a comprehensive analysis that accounts for differences across postsynaptic cells, we used linear mixed-effects (LME) modeling³⁴, with the postsynaptic cell as a random effect (see Methods for details). This analysis indicated that, indeed, STP increased with increasing (absolute) excEPSC amplitude of excitatory connections (0.011 per 100 pA \pm 0.012 SE, $\chi^2(1) = 6.4$, $P = 0.012$; likelihood ratio test), and that STP decreased with increasing (absolute) inhEPSC amplitude of inhibitory connections (-0.031 per 100 pA \pm 0.010 SE, $\chi^2(1) = 6.8$, $P = 0.0089$; likelihood ratio test). These results were consistent with individual linear regression fits, which were separately calculated based on the connection data of each postsynaptic neuron (**Fig. 4b**). The identified approximately linear relationship between STP and connection strength indicated that the degree of input correlation was typically similar

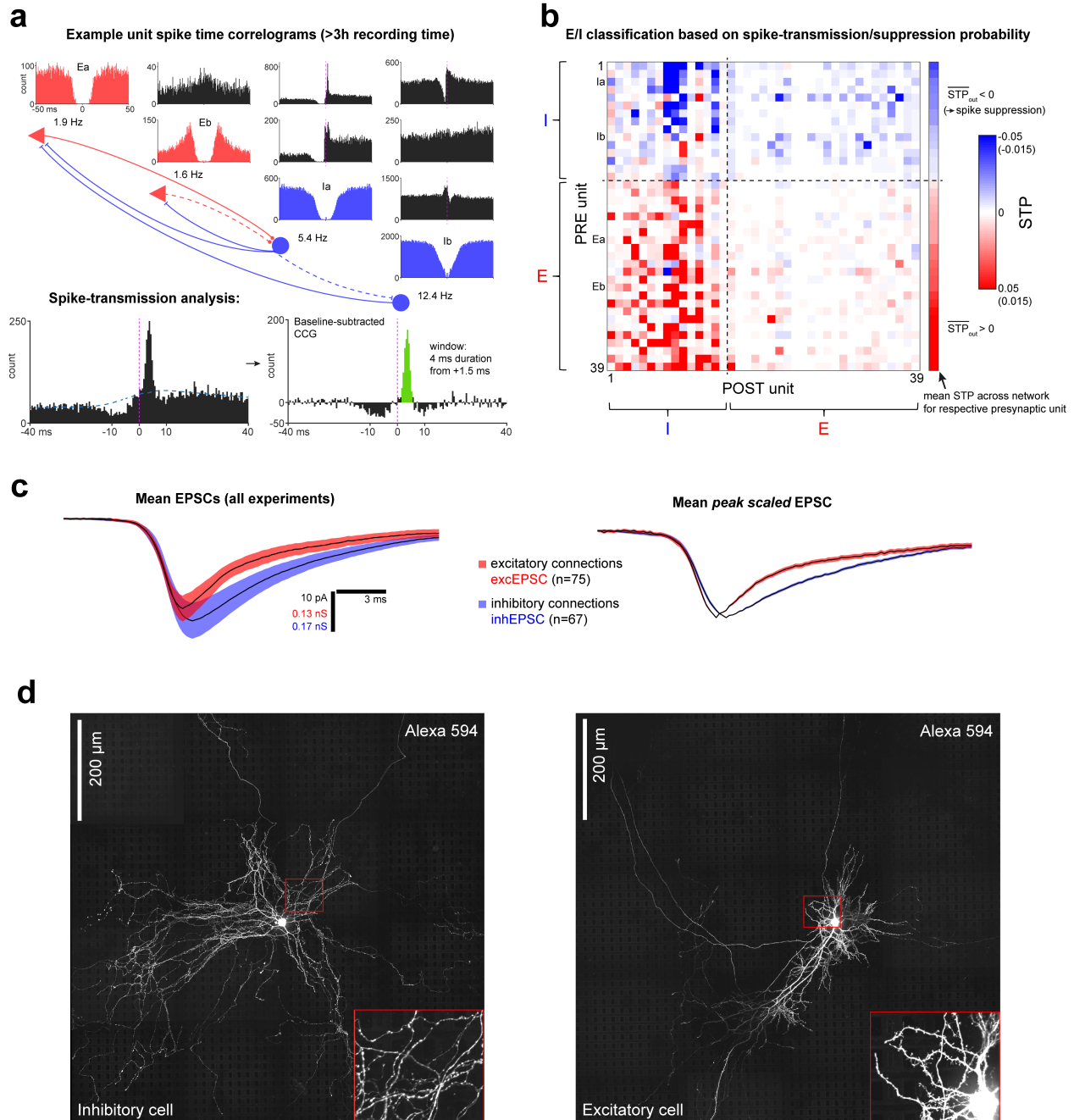


Figure 3. Connection-type classification based on network-wide spike transmission or suppression

(a) Top: auto- (red, excitatory cell; blue, inhibitory cell) and cross-correlograms (CCG; black) for four example units from a long-term HD-MEA recording (> 3 h). The schematic indicates putative connections based on the displayed CCGs (dashed lines for weak connections). Bottom: illustration of spike-transmission probability (STP) extraction. The dashed blue line (left) indicates the CCG baseline.

(b) Example matrix of STP values for all pairwise combinations of presynaptic units – as identified by our regression approach – and postsynaptic units from a long-term HD-MEA recording. The rows labeled Ia/b and Ea/b correspond to the units shown in (a). In each row, one specific unit is the reference (or ‘presynaptic’) unit in the cross-correlation, and the other units sequentially represent the target (or ‘postsynaptic’) units (diagonal values were set to zero). The mean STP (across the sub-network) for each reference unit is shown on the right. Units are classified as being putatively excitatory or inhibitory based on the sign of their mean STP value. The color scale was chosen for better overall visibility and some STP values are outside the displayed range. The color scale values in brackets apply to the column of mean STP values. Note the relatively large STP values associated with E-I compared to E-E unit pairs – in line with strong E-I connections typically found in the cerebral cortex³¹.

(c) Left: mean peak-aligned EPSCs, pooled from all experiments (14 patched cells) for connections that were classified to be excitatory ($n = 75$; decay $\tau_{fast} = 2.5$ ms, $\tau_{slow} = 15.2$ ms) or inhibitory ($n = 67$; decay $\tau = 8.6$ ms). EPSC estimates for excitatory and inhibitory connections are referred to as ‘excEPSCs’ and ‘inhEPSCs’, respectively. Right: same as on the left, but individual EPSC waveforms were first normalized with respect to their peak amplitude. Shadings denote the SEM.

(d) Large field-of-view fluorescence images of a putative inhibitory and excitatory cell (Z-projections of stitched mosaic of stacks; Alexa 594 loaded via patch pipette).

across the connections received by individual postsynaptic cells during spontaneous recurrent activity. Two additional observations are worth pointing out. For one, there were considerable differences in regression-line slopes across the different postsynaptic cells, implying that connections of similar strength can have varying, cell-dependent effects on spiking. Furthermore, many of the (relatively weak) excitatory connections, remarkably, exhibited STP values scattered around zero, while inhibitory inputs had generally a more reliable (suppressive) effect on postsynaptic spiking. The results of this section indicated that inhibitory connections were particularly important for the control of spike timing.

Networks operate in a fine-tuned dynamical regime governed by rapid input changes

To elucidate the synaptic basis of postsynaptic spiking during spontaneous recurrent network activity, it is necessary to consider – in parallel – the combined excitatory and combined inhibitory conductances generated by the incoming connections. We reconstructed the synaptic activity experienced by the postsynaptic (patched) cells during the long-term extracellular recording period that preceded the patch-clamp experiments, as depicted in **Fig. 1a** (see Methods for details). The observed alternations at the network level between periods of sparse spiking and periods of heightened, self-maintained network activity (see **Fig. 1c/f**) manifested as alternations between low and high conductance states (**Fig. 5a**). Synaptic conductances were often approximately balanced, with inhibitory conductance (g_i) typically exceeding the excitatory conductance (g_e), similar to estimations of the conductances generated by spontaneous network activity in vivo²⁶ and in vitro³⁵.

The parallel reconstructions of the g_e and g_i traces also allowed us to calculate the E/I ratio during spontaneous network activity; here quantified as $E/(E+I)$ (black trace, right, in **Fig. 5a**). Remarkably, this trace directly revealed brief spikes in the E/I ratio, during which postsynaptic action potentials preferentially occurred. We also assessed the temporal characteristics of the synaptic inputs in more detail (**Fig. 5b**). This analysis revealed, on average, a brief lag between excitation and inhibition and uncovered, particularly for inhibitory inputs, oscillatory dynamics, as observed in cortical and hippocampal networks in vivo^{22, 25, 26, 36}. Moreover, quantifying the pairwise spike-train synchrony between all presynaptic cells showed a higher synchronization of inhibitory cells compared to excitatory cells, although overall the degree of pairwise neuronal synchrony was only moderate (**Fig. 5c**).

To examine which synaptic events determine postsynaptic spiking, we subsequently generated the spike-triggered average of the inhibitory ($g_{i,STA}$) and excitatory input conductance ($g_{e,STA}$) for each postsynaptic cell. This analysis showed that both a rapid decrease in inhibition or a rapid increase in excitation could be the

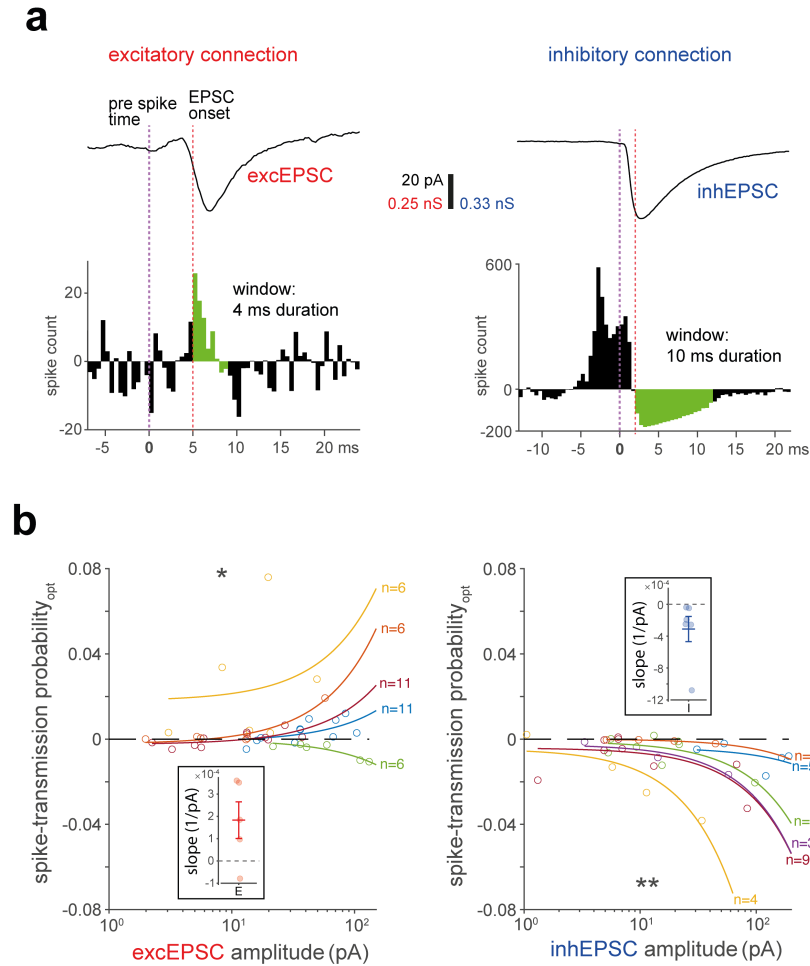


Figure 4. Relationship between connection strength and STP at single postsynaptic-cell level indicates crucial role for few strong connections in spike timing

(a) Optimization of STP estimates. Bottom: example baseline-subtracted CCGs, based on spike trains of a presynaptic and the postsynaptic unit. Top: EPSC of the corresponding connection. The EPSC onset latency relative to the presynaptic spike time was used to set the start time of the STP quantification window (green), thereby providing a more accurate STP estimate. This approach was particularly important for excitatory connections with variable excEPSC onset latencies; e.g., due to variable axonal length or synapse location within the dendritic tree.

(b) Relationship between STP (optimized estimate) and EPSC amplitude for excitatory (left)/inhibitory (right) connections onto individual postsynaptic cells; lines are linear fits (here curves because of the logarithmic axis for amplitude; data points and linear fit belonging to the same postsynaptic cell are displayed in the same color). Insets show slopes from the linear fits with mean \pm SD. Only cells with at least three E/I inputs were included ([E/I] 5/6 cells and 40/33 connections). Across all connections, the mean STP value for excitatory and inhibitory connections was 0.0025 ± 0.0150 SD and -0.0090 ± 0.0099 SD, respectively. Data were comprehensively analyzed by linear mixed-effects modeling (with EPSC amplitude as a fixed effect and postsynaptic cell ID as a random effect).

Significance was assessed by a likelihood ratio test. * $P < 0.05$, ** $P < 0.01$

primary trigger of action potential firing (**Fig. 5d**). In addition, postsynaptic spiking consistently coincided with a rapid increase in inhibitory input conductance, thereby constraining the window of opportunity for spike generation. The STA conductances could also be calculated separately for each incoming connection, which revealed a large spectrum of input-specific conductance profiles associated with postsynaptic spiking (**Supplementary Fig. 3**). The fact that spike timing was often precisely controlled by rapid changes in synaptic input conductances was also reflected in the E/I ratio of the average conductances (black traces in **Fig. 5d**). For 7 out of 9 postsynaptic neurons, we found a fast increase in the input $E/(E + I)_{STA}$ before postsynaptic spiking (**Fig. 5e**). These findings strongly suggest that the networks and neurons operated, at least partially, in a dynamical regime governed by rapid input changes. A quantification of the contributions of excitation and inhibition to the fast $E/(E + I)_{STA}$ increases (from 30%-70% of the peak amplitude) further showed that, across recordings, both an increase in excitation and a decrease in inhibition contributed significantly (**Fig. 5f**). For 5 out of 7 cells, the contribution of a reduced inhibition exceeded an increase in excitation (however, no significant difference in the contributions was found). Finally, we uncovered the temporal relationship between the input $E/(E + I)_{STA}$ and the intracellular action potential waveform. To this end, we conducted additional paired HD-MEA and IC patch-clamp recordings during spontaneous spiking of the patched cell, which allowed for extracting the temporal relationship between extracellular spike times, as determined by our spike-sorting procedure, and the intracellularly recorded action potential (**Supplementary Fig. 4**). Subsequently, we could align the mean E/I ratio change from **Fig. 5e** to the intracellular action potential waveform (**Fig. 5g**). The aligned mean input-output data showed that the peak of the rapid E/I ratio increase coincided precisely with the action potential trigger time point. This observation suggested a fine-tuned network organization, presumably with an important role for feed-forward inhibition.

Coordination of postsynaptic spiking by inhibitory inputs is sharpened during high-activity states

Different network-activity levels presumably provide distinct means for the coordination of neuronal activity, with potential implications for the synaptic mechanisms of spiking. We, therefore, examined if the network state would influence the mean input conductances that were associated with postsynaptic spiking, and we focused on the dominant changes in inhibitory inputs (**Fig. 6**). Specifically, we calculated the spike-triggered average conductances separately based on postsynaptic spike times that occurred either during high or low input conductance states (high g state, when $g_i > 3 \times$ s.d. of g_i trace, otherwise low g state; high g periods corresponded to high-activity events, such as the one depicted in **Fig. 5a**, right). Both low and high $g_{i,STA}$

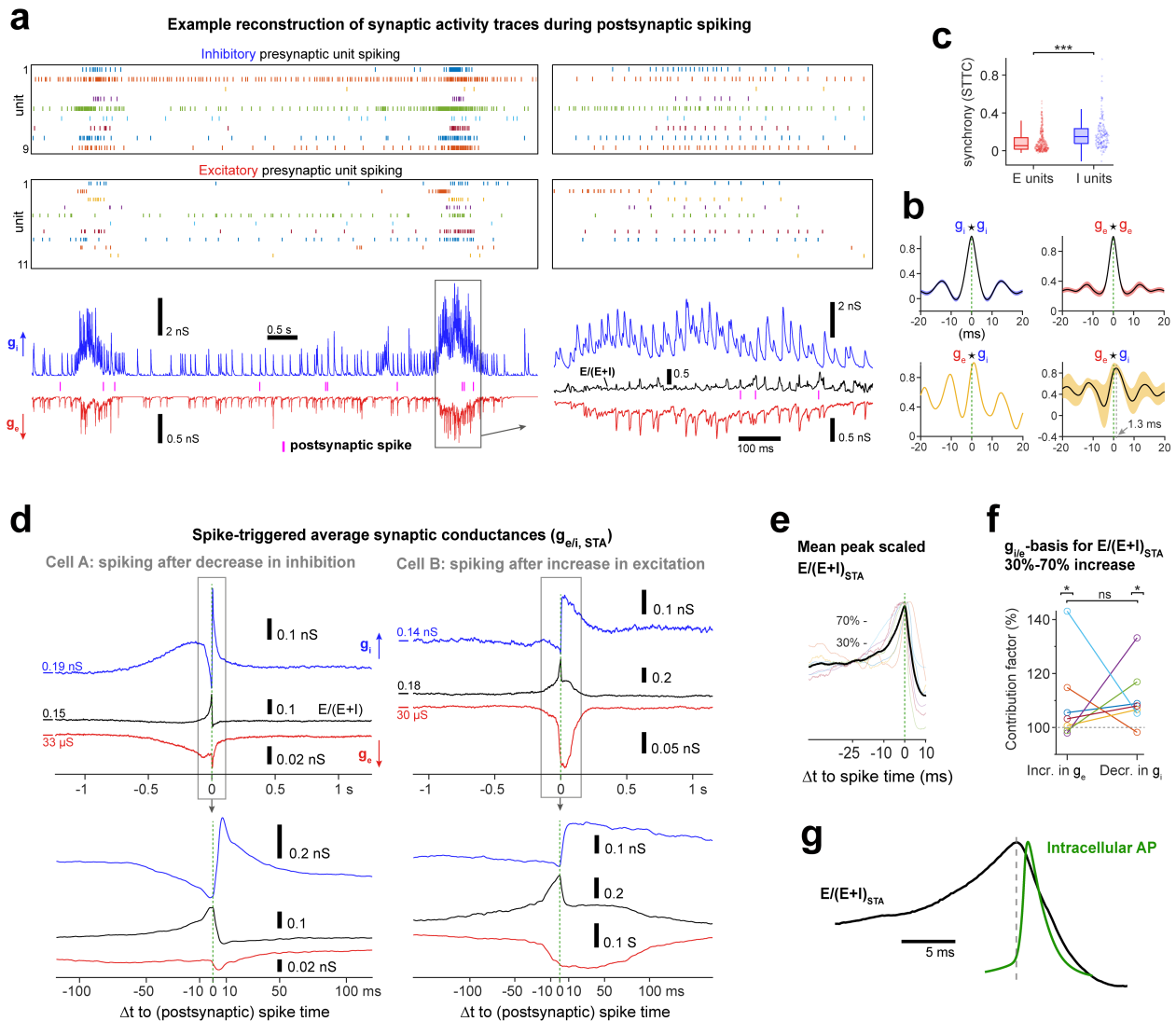


Figure 5. Networks operate in a fine-tuned dynamical regime governed by rapid input changes

(a) Top: raster plot of spike times for all inhibitory and excitatory presynaptic units of an example postsynaptic cell. Bottom: reconstructed inhibitory (g_i ; blue) and excitatory (g_e , red) synaptic conductance traces. Spike times of the postsynaptic unit in magenta. For the enlarged high-conductance period (right), the $E/(E+I)$ ratio is also displayed (black trace).

(b) Mean auto- (ACG) and cross-correlograms (CCG) of the reconstructed g_i and g_e of the neuron in (a) (25 individual mean-subtracted high-conductance events). For $g_e * g_i$, also one individual high-conductance event shown.

(c) Pairwise unit synchrony (quantified by the spike time tiling coefficient [STTC] with 10 ms binning³⁷) of all presynaptic units recorded in parallel ([E/I] 330/168 unit comparisons; $U = 16288$, $P < 0.001$, Mann-Whitney U test).

(d) Example spike-triggered average of synaptic input conductances and $E/(E+I)$ ratio of two neurons. The sharp increase in $E/(E+I)$ just before the postsynaptic AP was dominated by either a disinhibition (left; $n = 15'813$ synaptic events) or an increase in excitation (right; $n = 1'730$ events).

(e) Mean (black) and individual baseline-subtracted (-30 to -20 ms) and peak scaled spike-triggered average $E/(E+I)$ traces ($n = 7$ out of 9 cells with mean E/I ratio from -5 to 0 ms $> 3 \times$ standard deviation (s.d.) of baseline).

(f) $g_{e/i}$ -basis for the $E/(E+I)_{STA}$ increase from 30-70% of the peak amplitude. The g_e contribution was quantified as $c_e = g_{e,70\%}/g_{e,30\%}$ and the g_i contribution (decrease in inhibition) was quantified as $c_i = g_{i,30\%}/g_{i,70\%}$, with the relative E/I increase from 30-70% given by $c_e \times c_i$. Both g_i and g_e significantly contributed to the $E/(E+I)_{STA}$ increase ($Z = 2.4$, $P = 0.018$, for both, Wilcoxon signed rank test compared to zero) with no significant difference between the contributions ($Z = -0.51$, $P = 0.61$, Wilcoxon signed rank test).

(g) $E/(E+I)_{STA}$ (black; mean from (e)) aligned to intracellular AP (green; mean from Supplementary Fig. 4).

Shadings in (b) denote SEM. Box plots in (c) indicate median and interquartile ranges, and whiskers the minimum/maximum values except for outliers. * $P < 0.05$, ** $P < 0.01$, *** $P < 0.001$.

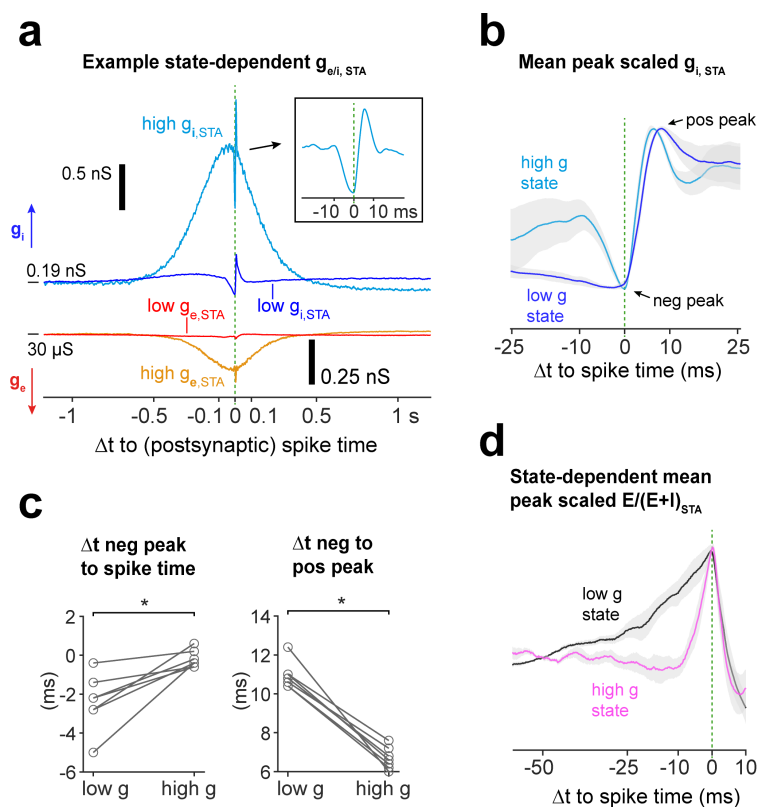


Figure 6. Coordination of postsynaptic spiking by inhibitory inputs is sharpened during high-activity states

(a) For an example postsynaptic cell, spike-triggered average synaptic conductances ($g_{e/i,STA}$) based on postsynaptic spike times that occurred during periods of either high ([E/I] orange/light-blue) or low (red/blue) input conductance states. The inset shows a detailed view of the high $g_{i,STA}$ trace around postsynaptic spike time.

(b) Mean $g_{i,STA}$ across experiments ($n = 7$ postsynaptic cells) for high (light-blue) and low g (blue) states; scaled by their respective negative and positive peak values.

(c) Comparison of the time difference between the negative $g_{i,STA}$ peak and postsynaptic spike time ($Z = -2.4$, $P = 0.018$, Wilcoxon signed rank test) and the time difference between the negative and positive $g_{i,STA}$ peaks ($Z = 2.4$, $P = 0.018$, Wilcoxon signed rank test) for low and high g states.

(d) State-dependent $E/(E + I)_{STA}$ across experiments ($n = 7$; traces baseline subtracted and peak scaled).

Shadings in (b) and (d) denote SEM. * $P < 0.05$.

traces exhibited the characteristic bidirectional shape with a reduction in inhibition before the postsynaptic action potential, followed by a rapid increase in conductance (Fig. 6a/b). However, when comparing the temporal $g_{i,STA}$ trace characteristics, it became apparent that the high $g_{i,STA}$ conductance changes occurred considerably faster (Fig. 6c), which also manifested as sharpened $E/(E + I)_{STA}$ peaks associated with high g states (Fig. 6d). These results, likely a consequence of the temporal coordination of inhibitory cells, suggest an increase in the precision of postsynaptic spike timing during the neuronal high-conductance states associated with heightened network-activity levels.

Organization of incoming monosynaptic connections at the level of individual postsynaptic cells

Having investigated the synaptic conductances that underlie the control of spike timing, we next examined the organization of the neural circuits that supported the observed spiking regime. Specifically, we characterized, from the perspective of individual postsynaptic cells, the distributions and relationships of key properties (synaptic strength, spike rate and EPSC onset delay) of the incoming monosynaptic connections (Fig. 7). A fundamental aspect of neural network organization is the fact that the distributions of network properties are often best characterized by a log-normal function, which has been linked to optimal information storage

and processing principles^{38,39}. First, we tested if the methods developed in the previous sections could reveal similar organizational principles in our neuronal culture model. We pooled the connection data from all recordings; and indeed, the distributions of all properties, with the exception of inhibitory onset latency, were well described by a log-normal distribution (left panels in **Fig. 7b-d**). Moreover, all properties showed significant differences between excitatory and inhibitory connections. Consistent with typical in vivo findings, inhibitory cells displayed higher spike rates and conductances and lower onset latencies compared to excitatory cells, indicative of a relatively strong and fast action of inhibition. The fast inhibition (i.e., small onset latencies) was likely the result of both a relatively local inhibitory innervation and a fast axonal action potential propagation (**Supplementary Fig. 2**).

How are the properties of incoming connections organized from the perspective of individual postsynaptic cells? Are distributions skewed, as observed at the network level, or more homogeneous? Even though the nature of these property distributions would provide important insights into neural functioning, experimental single-cell data and corresponding characterizations are scarce. We, therefore, used our data sets to calculate the skewness s , for each postsynaptic cell and each incoming connection property (right panels in **Fig. 7b-d**; a log-normal distribution is associated with a positive skewness). Synaptic strength and spike rate were typically associated with a positively skewed distribution at the single (postsynaptic)-cell level. These results suggested that individual neurons were particularly strongly influenced by a few key inputs, while the majority of incoming connections played – individually – a relatively small role.

Finally, we examined – at the level of individual postsynaptic cells – the relationships between connection strength (i.e., absolute EPSC amplitude) and either the EPSC onset latency or the presynaptic spike rate. Uncovering these relationships may provide indications of the regulatory processes of synaptic strength that were implemented by the networks. We fitted individual linear regression lines for each postsynaptic cell (**Fig. 7e/f**) and performed a comprehensive analysis across cells using linear mixed-effects (LME) modeling. We found that for most postsynaptic cells, the strength of incoming inhibitory connections decreased with increasing onset latency, and the relationship was well characterized by linear regression fits (**Fig. 7e**; according to LME model: $-14.2 \text{ pA} \pm 2.8 \text{ SE per ms}$, $\chi^2(1) = 13.1$, $P < 0.001$; likelihood ratio test). This result provided further evidence that individual postsynaptic cells were dominated by strong local inhibition. Furthermore, the strength of excitatory connections decreased with increasing presynaptic spike rate, and the relationship was well described by an exponential decay (**Fig. 7f**; amplitude values were linearized by log-transformation; according to LME model: $-8.4 \% \pm 3.2 \text{ SE decrease in amplitude per Hz}$, $\chi^2(1) = 4.8$, $P = 0.029$). This finding indicates a homeostatic synaptic plasticity mechanism so as to achieve a downregulation of synaptic strength for connections that were particularly active.

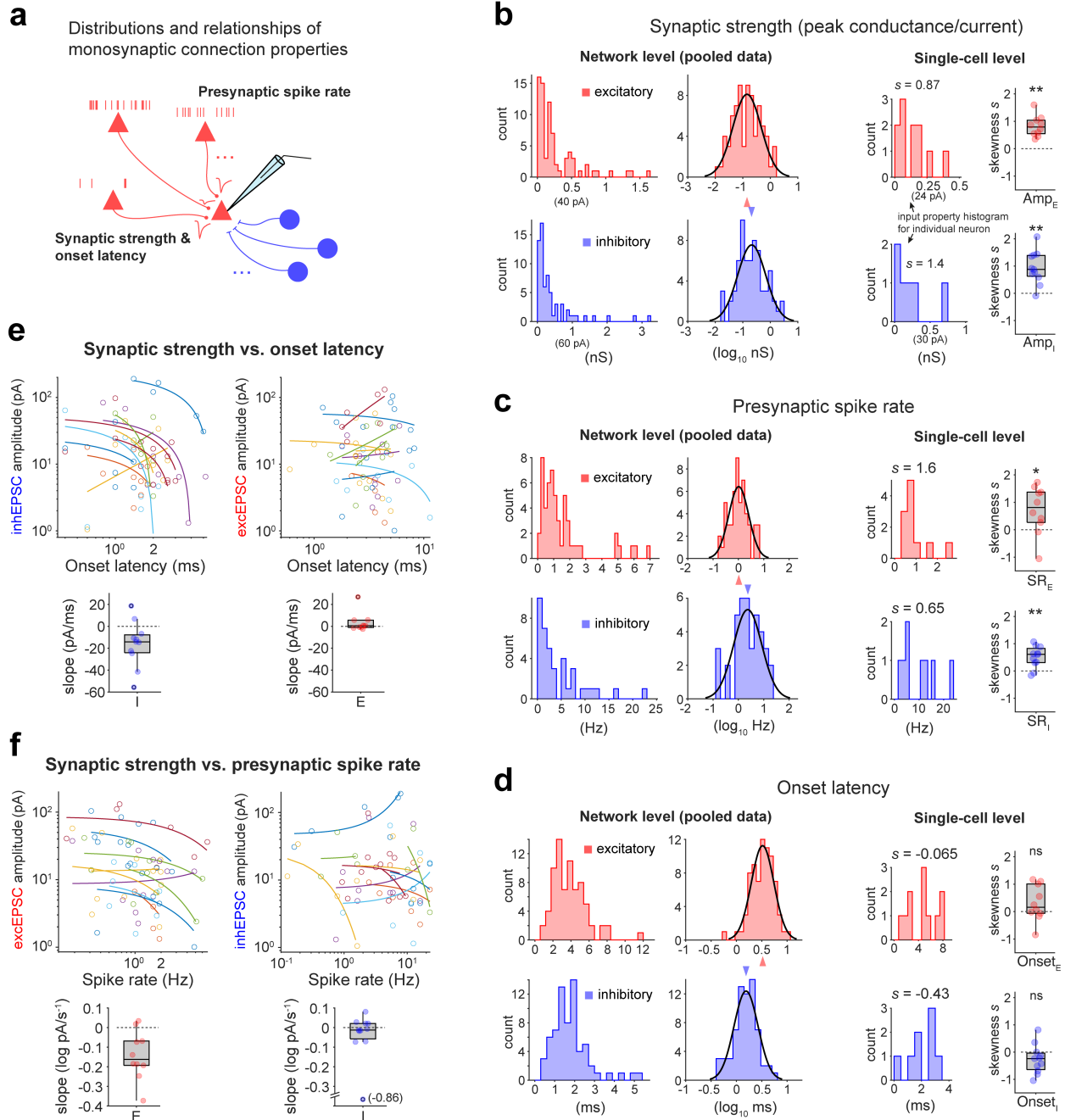


Figure 7. Organization of incoming monosynaptic connections at the level of individual postsynaptic cells

(a) Presynaptic spike rate, amplitude of the EPSC estimate (also converted to conductance) and EPSC onset latency were analyzed, separately, for excitatory and inhibitory connections.

(b-d) For each property, data were examined at the network level (connections from all 14 paired recordings pooled) and from the perspective of the individual postsynaptic cells. For the network-level analysis (left), a histogram with and without previous log-transformation is shown (black curve: Gaussian fit; arrow head marks the peak). For all properties, including amplitude ($U = 1660$, $P < 0.001$, $n[E/I] = 75/67$), spike rate ($U = 601$, $P < 0.001$, $n[E/I] = 45/33$, common presynaptic units only included once) and onset latency ($U = 739.5$, $P < 0.001$, $n[E/I] = 75/67$), there was a significant difference between excitatory and inhibitory connections (Mann-Whitney U test). Moreover, all distributions, except for that of inhibitory onset latency (d), were approximately log-normal according to a Shapiro-Wilk test. For the single-cell-level analysis (right), an example single-cell histogram is shown in addition to a box plot of the skewness s for each incoming connection property (one skewness value for each postsynaptic cell). The skewness of amplitude ($[E/I]$; $Z = 2.8/2.8$, $P = 0.0051/0.0044$, $n = 10/11$ postsynaptic cells) and spike rate ($[E/I]$; $Z = 2.1/2.7$, $P = 0.037/0.0076$), but not onset latency ($[E/I]$; $Z = 1.4/-1.5$, $P = 0.17/0.13$), was significantly different from zero (Wilcoxon signed rank test). For all single-cell level analyses, only cells with at least 3 E/I inputs were included ($n[E/I] = 10/11$ cells).

(e) Relationship between EPSC amplitude and onset delay at single-cell level. Top: scatter plot, with one linear regression fit for each postsynaptic cell (here curves, because of logarithmic axes for better data visibility). Bottom: slope values of linear fits.

(f) Relationship between EPSC amplitude and presynaptic spike rate at the single-cell level. Amplitude values were log-transformed, otherwise as in (e).

Data in (e/f) were comprehensively analyzed by linear mixed modeling. Significance was assessed after applying the Holm correction for multiple comparisons. Box plots indicate median and interquartile ranges and whiskers the minimum/maximum values except for outliers. ns, not significant, $*P < 0.05$, $**P < 0.01$

A few key inhibitory hub cells with high spike rates, strong synapses and fast action potential propagation dominate the network

The results of the previous sections showed that individual neurons were particularly strongly influenced by a few connections with strong synapses (Fig. 7), which translated to strong effects on postsynaptic spiking (Fig. 4). Did the presynaptic neurons that provided these important inputs exhibit characteristic properties or were these inputs of random neuronal origin? To answer this question, we characterized the organizational principles concerning outgoing connections (Fig. 8). We focused on a network, in which multiple paired HD-MEA and patch-clamp recordings were sequentially obtained from different postsynaptic cells (Fig. 8a). Following the identification of incoming connections for each paired recording using our regression approach, we found that the same presynaptic cell formed often connections with multiple postsynaptic (patched) cells (see matching footprints in top inset in Fig. 8a and Supplementary Fig. 5). There was a variety of different outdegrees, with relatively few highly connected presynaptic cells (Fig. 8b). Individual presynaptic cells evoked EPSCs with drastically varying amplitudes in different postsynaptic cells (bottom inset in Fig. 8a), and the distribution of outgoing connection amplitudes was typically positively skewed (Fig. 8c). Next, we asked whether there was a relationship between the degree of outgoing connectivity and other neuronal properties that determine the cell's influence on the network. Indeed, for inhibitory – but not excitatory – cells, the spike rate of a neuron correlated with its outdegree (Fig. 8d). Furthermore, the sum of outgoing inhEPSC amplitudes of individual inhibitory cells increased rapidly with the outdegree, while for excitatory cells this increase was slower (left in Fig. 8e). To examine if the degree of outgoing connectivity influences the mean connection strength, we first calculated the mean postsynaptic EPSC waveform (\overline{EPSC}_{out}) for each

presynaptic cell. Subsequently calculating the mean waveform of all \overline{EPSC}_{out} from cells with outdegree 1-3 and 4-7, respectively, indicated that highly connected inhibitory – but not excitatory – cells formed particularly strong synapses with their postsynaptic targets when compared to cells with few outgoing connections (right in **Fig. 8e**). Finally, the action-potential propagation velocity of inhibitory cells (see Methods for details) also increased with the outdegree (**Fig. 8f**). In summary, a few key inhibitory cells were in a unique position to coordinate network activity by exerting fast and strong effects through an extensive network of outgoing connections.

Discussion

We examined the synaptic mechanisms that determine postsynaptic spike timing during spontaneous recurrent network activity – linking functional and organizational circuit characteristics. These investigations were made possible through several methodological innovations including a comprehensive synaptic input mapping in conjunction with long-term extracellular whole-network recordings, which allowed for reconstructing synaptic activity during a period of postsynaptic spiking. For the input-mapping approach, based on simultaneous HD-MEA and patch-clamp recordings, we developed and validated a regression procedure that inferred a large proportion of the (current-evoking) monosynaptic connections onto individual postsynaptic cells. Compared to even the most advanced multi-channel patch-clamp platforms^{31,40}, our approach exceeded the number of testable incoming connections by an order of magnitude.

During sensory stimulation and spontaneous network activity, neurons typically experience a proportional or ‘balanced’ change in excitatory and inhibitory inputs^{6-8,15}. Theory suggests that multiple dynamical regimes could yield this balance^{17,23}, and understanding the nature of the implemented regime is crucial for gaining a better understanding of cortical function in general. Theoretical and computational modelling studies further indicate that, during the balanced state, rapid membrane potential fluctuations could be the primary spike trigger¹⁶⁻¹⁹. These studies typically assume randomly connected networks with asynchronous irregular firing. It remains to be seen to what extent these findings hold true in biological networks with structured connectivity and – as often seen during spontaneous cortical activity – more synchronous spiking¹⁶. In addition, other dynamical regimes have been described, including spiking driven by the mean input rather than rapid input fluctuations^{23,24}.

Here, we directly tested in biological neural networks if postsynaptic spiking was associated with rapid changes in synaptic inputs. First, we showed that, for individual postsynaptic cells, the strength of excitatory and inhibitory connections correlated with the degree of postsynaptic-spike transmission and suppression, respectively. However, many of the spike-time cross-correlograms associated with excitatory connections did

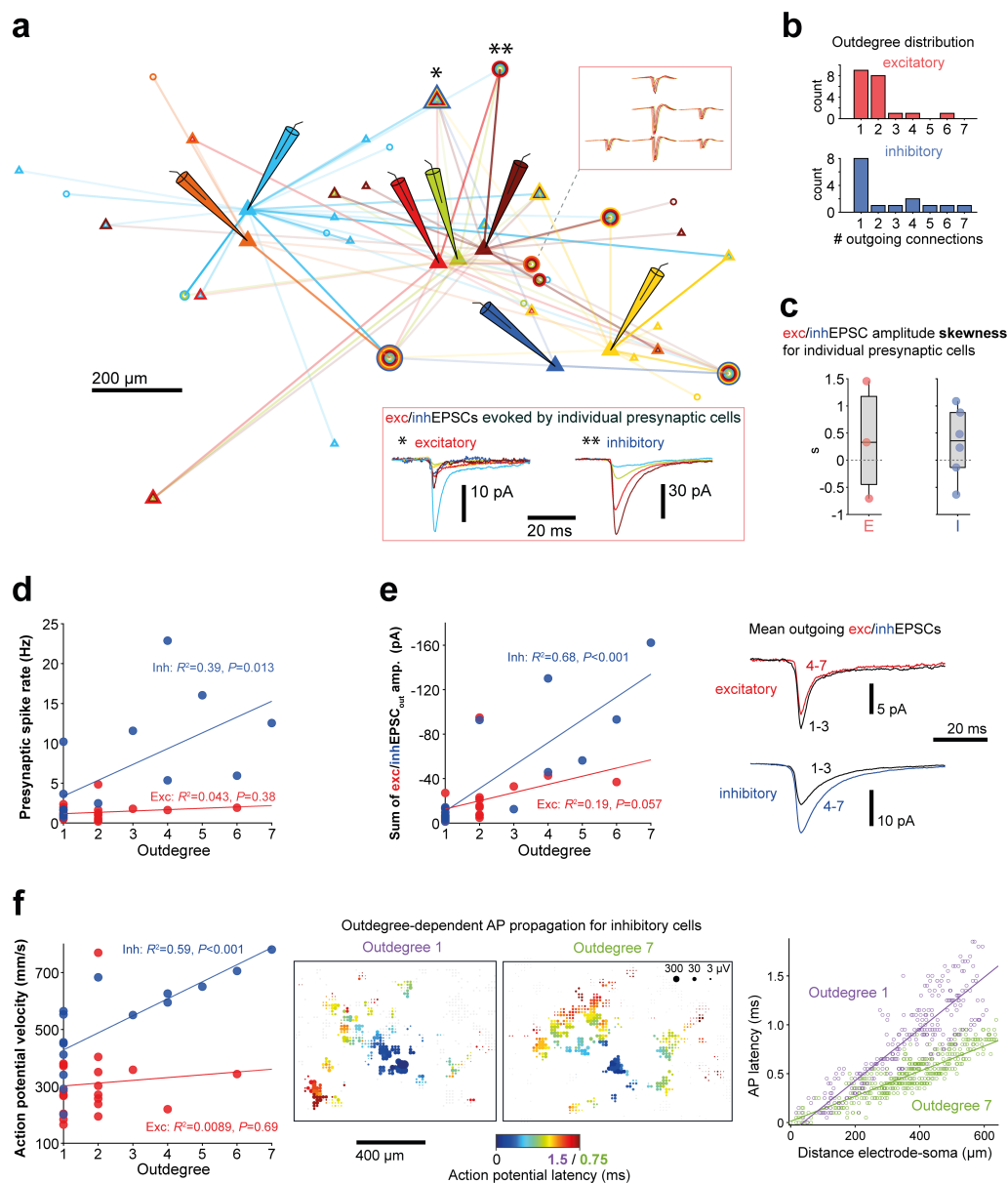


Figure 8. A few key inhibitory hub cells with high spike rates, strong synapses and fast action potential propagation dominate the network

(a) Multiple neurons in the same network were sequentially patched (cell position marked by microelectrode schematic). Paired patch-clamp and HD-MEA recordings were performed for each cell, followed by identification of their incoming connections using our regression approach. Open triangles and circles mark the positions of excitatory and inhibitory cells, respectively (plotted connection lines indicate synaptic strength: the more transparent the line, the weaker the connection). Overlaid circles/triangles represent neurons that were presynaptic to multiple patched cells. Top inset: virtually identical example extracellular footprints from four separate paired HD-MEA and patch-clamp recordings, in which the respective unit was found to be presynaptic to the patched cell (footprint traces slightly shifted in time for better visibility). Bottom inset: Example EPSCs evoked in different postsynaptic cells by the same excitatory/inhibitory presynaptic cell (marked in the network schematic by single/double asterisk). The positions of the blue, green and brown patched cell in the network schematic were approximations, as the postsynaptic footprint was not available.

(b) Outdegree distribution for the network shown in (a).

(c) Skewness s of the amplitude distribution of the outgoing connections for individual neurons (only presynaptic cells with at least 3 outgoing E/I connections were included).

(d) Relationship between the spike rate of a neuron and its outdegree. Significance was assessed after applying the Holm correction for multiple comparisons.

(e) Left: Relationship between the sum of EPSC amplitudes of all outgoing connections of a neuron and its outdegree. Right: for each presynaptic cell, the mean postsynaptic EPSC waveform ($EPSC_{out}$) was computed; the mean of all $EPSC_{out}$ from cells with outdegree 1-3 and 4-7 are shown.

(f) Left: Relationship between action potential velocity of a presynaptic neuron and its outdegree. Middle: Example HD-MEA action potential (AP) latency plot from a neuron with outdegree 1 and 7. Right: Plots of AP latency vs. distance between electrode and soma for the two example units.

not show clear peaks of excess spiking, which may indicate that these inputs provided more of a ‘basal excitatory tone’ and, hence, contributed to, but did not determine the precise timing of, membrane potential fluctuations. On the other hand, the spike-suppressive effect of inhibitory inputs was found to be generally reliable. In line with these results, the reconstruction of synaptic input conductances revealed that postsynaptic spiking often coincided with the peak of E/I ratio fluctuations. These changes in E/I ratio were – depending on the postsynaptic cell – primarily due to either an increase in excitation or decrease in inhibition, while the decrease in inhibition outweighed the increase in excitation in most cells. The finding that neurons have the ability to respond to different combinations of conductance changes is consistent with reports of dynamic-clamp experiments²⁷. We also showed that a rapid increase in inhibition typically restricts the spiking window and that the temporal characteristics of inhibition around the postsynaptic spike time is sharpened during periods of heightened network activity. The latter observation could stem from a synchronization of inhibitory neurons, as often observed *in vitro* and *in vivo*^{20–22}. In summary, we found that the studied biological networks were equipped with several mechanisms that allowed them to operate, at least partially, in a precise dynamical regime governed by rapid input changes. Interestingly, cortical neurons *in vivo* typically receive – in response to diverse sensory stimuli – stereotypical excitation-inhibition sequences and, in this scenario, the excitatory inputs presumably determine the initial timing of the depolarization^{25,41,42}. To consolidate these findings with the observed role for inhibition in controlling spike timing, it is conceivable that there are two main modes of neuronal spiking: external inputs trigger a depolarization due to an increase in excitation, while spontaneous spiking (e.g., associated with slow-wave sleep or neuronal cell-culture activity) is predominantly driven by local recurrent activity and, in particular, by a reduction in inhibition. It is an intriguing question to ask what the implications of these different spiking modes would be (e.g., for spike-timing dependent plasticity).

Finally, we investigated the circuit architecture that supported the observed spiking regime. Highly connected hub neurons are believed to be important for the coordination of network activity^{43–45}, but electrophysiological characterizations of their connections are scarce. Here, we also identified a minority of cells with high connection outdegrees. Moreover, we found that inhibitory cells that were highly connected were also fast-spiking and featured relatively strong synapses and fast action potential propagation velocities. In addition, when we examined the incoming connections onto individual postsynaptic cells, we found that connection strength and presynaptic spike rate followed approximately a log-normal distribution, implying that a few incoming connections were particularly dominant. Combining these findings on the organization of incoming and outgoing connections with our functional data, a picture emerges in which network-wide neuronal spiking is effectively coordinated by a few key inhibitory hub neurons with windows of spiking opportunity provided by a brief reduction in their postsynaptic effects.

The findings presented in this work provide a detailed characterization of a dynamical regime that is in line with theoretical predictions for neural networks in vivo. Our results were obtained in a cortical cell culture model and we, therefore, propose that a self-organization towards a dynamical regime governed by rapid input changes is an inherent property of cortical networks.

Methods

Primary neuron culture preparation

The experimental protocols involving animal tissue harvesting were approved by the veterinary office of the Canton Basel-Stadt according to Swiss federal laws on animal welfare and were carried out in accordance with the approved guidelines. Before cell plating, the HD-MEA chips were sterilized for 45 min in 70% ethanol and washed 3 × with sterile deionized (DI) water. Next, the electrode array was treated with 20 μL of 0.05% (v/v) poly(ethyleneimine) (Sigma-Aldrich) in borate buffer (Thermo Fisher Scientific) at 8.5 pH, for 40 min at room temperature, and then washed 3 × with DI water. Subsequently, we added 8 μL of 0.02 mg mL⁻¹ laminin (Sigma-Aldrich) in Neurobasal medium (Gibco) and incubated the chips for 30 min at 37 °C. Cortices of E-18 Wistar rat embryos were harvested in ice-cold HBSS (Gibco) and then dissociated in trypsin with 0.25% EDTA (Gibco). We next seeded 15'000 to 20'000 cells on top of the electrode array. Subsequently, the chips were incubated at 37 °C for 30 min before adding 2 mL of plating medium. The plating medium stock solution consisted of 450 mL Neurobasal (Gibco), 50 mL horse serum (HyClone, 1.25 mL Glutamax (Invitrogen), and 10 mL B-27 (Invitrogen). Every 3-4 days, 50% of the culture medium was replaced by growth medium, with the stock solution consisting of 450 mL D-MEM (Invitrogen), 50 mL horse serum (HyClone), 1.25 mL Glutamax (Invitrogen), and 5 mL sodium pyruvate (Invitrogen). The HD-MEA chips were kept inside an incubator at 37 °C and 5% CO₂. All the experiments were conducted between days in vitro (DIV) 15-18, when cellular growth and network connectivity had stabilized.

High-density microelectrode array (HD-MEA) system

A complementary-metal-oxide-semiconductor (CMOS)-based HD-MEA featuring 26'400 electrodes (pitch of 17.5 μm) within an overall sensing area of 3.85 × 2.10 mm² was used⁴⁶. An arbitrary subset of these electrodes could be connected to 1024 channels for simultaneous readout at 20 kHz sampling frequency. The HD-MEA system was developed in-house, but can also be purchased as the MaxOne model (MaxWell Biosystems). The electrodes were coated with electrodeposited platinum black to decrease electrode impedance and improve the signal-to-noise characteristics.

Electrode selection and long-term extracellular recording of network spiking

To select the HD-MEA electrodes for long-term recordings, all 26'400 electrodes were initially briefly scanned for activity (1 min per electrode). Electrodes that recorded spiking activity (minimum electrode spike rate: 0.05 Hz) were then identified and ranked according to their mean spike amplitude. Next, 2 or 3 × 1024 of

the electrodes with the largest signals were selected, which typically covered most of the active network. The selected electrodes were then divided into sets of up to 1024 electrodes along the longitudinal axis of the chip for simultaneous read-out (adjacent electrode sets had a small overlap of 3 electrodes width). To obtain long-term recordings of network spiking, we sequentially recorded from the electrode sets for 15 min each and repeated this every 1 h for a total recording time of at least 3 h for each electrode set.

Patch-clamp electrophysiology

For simultaneous patch-clamp and HD-MEA recordings, cultures were transferred immediately after the long-term network recording period from the incubator to a patch-clamp setup with integrated HD-MEA recording unit. From the the electrode sets that were used for long-term recordings, we then typically selected the electrode set covering the largest chip area with an even cell distribution and targeted pyramidal-shaped neurons towards the center of the electrode set for patching. The patch-clamp setup comprised a MultiClamp 700B amplifier (Axon Instruments) and an Axon Digidata 1440A (Axon Instruments). Data were low-pass filtered at 5 kHz and sampled at 20 kHz, with data acquisition controlled by the software WinWCP. Synchronization pulses were generated via the Digidata unit and fed into the HD-MEA system for post-recording data alignment. Cells were perfused with BrainPhysTM Neuronal Medium (Stem Cell Technologies) heated to approximately 32-34°C. Cell-attached and whole-cell patch-clamp recordings in voltage-clamp mode were obtained with standard borosilicate glass micropipettes (4–5 M Ω) containing the following internal solution (in mM): 85 caesium-gluconate, 60 CsCl, 10 HEPES, 4 Na₂ATP, 0.3 GTP, 2 MgCl₂, 0.1 EGTA, (pH 7.2–7.3; 280–290 mOsmol/l). Alexa Fluor 594 (20 μ M) (Sigma-Aldrich) was added for cell morphology assessment. The holding potential was set to -70 mV (without liquid-junction potential [LJP] correction). Only cells with a series resistance smaller than 25 M Ω were included in our study. We chose an internal solution with a relatively high chloride concentration, which causes a polarity reversal of GABA-A receptor-associated currents due to a more positive reversal potential (similar to early developmental periods). This approach allowed us to simultaneously record postsynaptic currents evoked by both GABAergic and glutamatergic synapses. We calculated the chloride reversal potential to be approximately -20 mV using the Nernst equation. Therefore, we used driving forces of 60 mV (inhibition) and 80 mV (excitation) to convert the synaptic currents to conductances according to Ohm's law (with a -10 mV LJP correction). The fact that both GABAergic and glutamatergic presynaptic neurons evoked EPSCs in the patched cells meant that a way to distinguish between the connection types was required. Typical excitatory-inhibitory classification strategies for 3D tissue, based on unit extracellular signatures and spiking behavior^{30, 47, 48}, appear to be not always sufficient for 2D preparations⁴⁹. We, therefore, performed a connection-type classification by assessing if a given

neuron's activity is typically associated with spike transmission or suppression.

For paired IC patch-clamp and HD-MEA recordings to examine the relationship between extracellular and intracellular action potentials and for dye loading to image neurites at high-resolution, the following internal solution was used (in mM): 110 potassium-gluconate, 10 KCl, 10 Hepes, 4 MgATP, 0.3 GTP, 10 phosphocreatine, (pH 7.2-7.3; 280–290 mOsmol/l). On the day of the experiment, Alexa Fluor 594 (20 μ M and 50 μ M for paired recordings and imaging experiments, respectively) was added.

To generate the spike-triggered average HD-MEA footprint of the patched cell, we used spontaneous spiking recorded in cell-attached mode or during a brief IC whole-cell recording. Additional spikes were sometimes triggered via current injection to increase the total number of spiking events.

Confocal fluorescence microscopy

A Nikon NiE upright confocal microscope featuring a Yokogawa W1 spinning disk, an ORCA-Flash4.0 V2 Digital CMOS camera (Hamatsu Photonics), and a 60x/1.00 NA water-objective (Nikon) was used for fluorescence imaging. To generate large field-of-view fluorescence images of neurite projections at high-resolution, individual neurons were loaded with Alexa Fluor 594 via the patch-pipette for at least 30 min. Multiple imaging tiles covering most of the cell morphology were defined. For each tile, a z-stack of images was acquired (0.4 μ m z-step; 0.1125 μ m x-y resolution). Using Huygens Professional (version=21.10; Scientific Volume Imaging), images were first deconvolved (CMLE algorithm) and then stitched together (10% overlap, circular vignetting correction model). A 561 nm excitation laser was used in combination with a 609/54 nm emission filter. To image the distribution of neurons on the HD-MEA chips, cultures were transduced with floxed EGFP (AAV9/2-hSyn1-chI-loxP-EGFP-loxP-SV40p(A); MOI = 5×10^5 vg) and Cre (AAV9-hSyn-Cre-WPRE-hGH; MOI = 5×10^4 vg) AAVs on DIV 7. A 488 nm excitation laser in combination with a 525/50 nm emission filter was used for EGFP imaging.

Processing of extracellular data

The extracellular data from the long-term recording period and from the paired HD-MEA and whole-cell patch-clamp recording were spike sorted with SpyKING Circus (version=0.8.4; parameters: spatial radius considered=210 μ m, width of templates=3 ms, spike threshold=6, cut-off frequencies for band-pass Butterworth filter=300 Hz/9500 Hz). For long-term data, the 15 min recording chunks from each electrode set were concatenated (yielding a total recording time of at least 3 h) and separately spike sorted. The HD-MEA data of the paired recordings for synaptic input estimation, were separately spike sorted, followed by manual curation with the SpyKING Circus curation interface (using template similarity and spike time cross-correlogram

characteristics as merging criteria). This procedure typically yielded clean units, based on which the synaptic input waveform estimation was performed. It was a robust approach, because even if some noise units with random spiking were retained, these units would likely be removed as there was no correlated postsynaptic activity. Moreover, if – in rare cases – two units had not been correctly merged, this would be revealed by input waveform estimates with very similar characteristics. Finally, the (presynaptic) units that were found to form a connections to the patched cell and the postsynaptic unit had to be identified in the long-term recording data. The HD-MEA footprint of the postsynaptic cell was generated by spike-triggered averaging (see Fig. 1e). For each of the presynaptic footprints and the postsynaptic footprint, we identified the corresponding best-matching footprints in the spike sorted long-term recording data (by using the maximum of the normalized cross-correlation between footprints). For almost all footprints, a clear match was found, and the unit was curated as above; only for very few individual footprints there was no match, and the respective connection was then excluded. An additional indication of the quality and validity of the spike sorting and footprint-matching procedures is given by the paired HD-MEA and IC whole-cell patch-clamp experiments (see Supplementary Fig. 4). The extracellularly detected spike times of the identified postsynaptic unit matched the intracellularly recorded action potentials well, which held even true for high-activity periods with some variations in action-potential shapes.

Regression approach for the estimation of synaptic input waveforms based on paired HD-MEA and patch-clamp recordings

We estimated synaptic input waveforms (e.g., EPSCs) by least squares linear regression of the whole-cell patch-clamp trace on simultaneously recorded unit spike trains according to equation 1 (see results section). Before running this estimation procedure, a preprocessing step to detrend the patch-clamp trace was applied. This was necessary as slow fluctuations appear as baseline shifts when short windows of the length of a single EPSC are concerned. These baseline shifts hinder the proper estimation of the waveforms. Briefly, the patch-clamp current trace was first down-sampled to 5 kHz and subsequently detrended. Detrending involved two steps. In the first step, very slow fluctuations in the current trace were determined using a sampling stride of 100 and applying a 20k-order median filter. The filtered trace captured very slow baseline drifts and was subsequently subtracted from the current trace. We call the modified current trace after this first detrending step S_{det1} . For the second detrending step, periods of high synaptic activity in S_{det1} were first detected (current deviations $> 3 \times$ s.d. of S_{det1}) and replaced by the median value of the entire S_{det1} trace. The remaining slow fluctuations were then determined by applying a 3k-order median filter to this modified S_{det1} trace. The resulting baseline trace was subtracted from S_{det1} , which yielded the fully detrended current trace.

The advantage of this two-step detrending procedure is that slow baseline fluctuations can be determined, even though the current trace features periods of high synaptic activity (e.g., due to network bursting). The preprocessing steps were applied to all VC whole-cell current traces shown here.

To verify that the preprocessing modifications to the current trace did not introduce major alterations in the EPSC waveform estimates, we developed an alternative approach for EPSC estimation based on spike-triggered averaging (STA) of isolated events (see **Supplementary Fig. 6** and methods section below). The STA method identified drastically fewer connections, but did not require a modification of the current trace. The EPSC estimates of connections that were identified by both the regression and STA method matched well (**Supplementary Fig. 6c**), suggesting that the effects of the preprocessing steps on waveform estimation were negligible.

A decisive advantage of our regression approach is that overlapping postsynaptic responses can be included in the EPSC waveform estimation. However, there are potential reasons (e.g., computational costs and non-linear interactions) to not include the most active periods of network spiking, which are associated with large postsynaptic currents. We evaluated the effect of different current thresholds, that determined which parts of the patch-clamp recordings were included in the regression analysis, and found $30 \times$ s.d. of the current trace to be a good compromise, which was therefore used for all recordings (**Supplementary Fig. 7**).

In the final step to estimate EPSCs, the spike trains of all units in the network with at least 10 spikes were encoded in a sparse binary u-by-t matrix (u: number of units; t: number of sampling points in the down-sampled current trace). Based on this spike time matrix and the preprocessed patch-clamp current trace, synaptic input waveforms were estimated with the *estimWaveforms* function of *Pillow et al. 2013* (URL: <https://github.com/pillowlab/BinaryPursuitSpikeSorting>). The waveform estimates included a 50 ms baseline period before the presynaptic spike occurred. Units were accepted to form a monosynaptic connection with the patched cell when the absolute EPSC amplitude $> 10 \times$ s.d. of the baseline. Virtually all of these waveforms exhibited a typical EPSC shape (fast rising and slow decay phase; very few individual traces that clearly deviated from this shape were removed).

We chose here voltage-clamp recordings of synaptic currents as the basis for the synaptic input estimation in order to minimize effects of non-linear interactions and due to the fast EPSC kinetics. The input estimation, however, can also be performed based on current-clamp recordings of postsynaptic potentials (**Supplementary Fig. 8**). For the estimation of EPSP waveforms, the procedure was the same as for EPSCs estimation except that only the first detrending step was performed (due to the relatively slow kinetics of synaptic potentials). Moreover, all recording periods with a voltage deviation up to 20 mV from baseline were included in the regression analysis, which excluded periods with postsynaptic action potential firing and strong synaptic activity.

Our MATLAB code that implements all preprocessing steps and the regression procedure is available at: https://github.com/neuroju/mea_patch_mapping.

Validation of regression approach by simulation of ground-truth synaptic inputs

To simulate ground-truth synaptic inputs, we generated artificial presynaptic spike trains and accordingly added a defined EPSC waveform to our measured patch-clamp current traces. The defined EPSC was the mean waveform of the (onset-aligned) EPSCs from all monosynaptic connections that were identified for the given postsynaptic (patched) cell. The entire EPSC waveform was scaled to achieve a desired EPSC amplitude. The EPSC estimation performance is likely to be influenced by the time periods (e.g., periods of heightened vs. low network activity) during which the EPSCs occurred. Therefore, trains of simulated presynaptic spike times were generated in a semi-random manner as follows: First, for each paired HD-MEA and patch-clamp recording, the measured spike times from all units in the network were combined and binned (100 ms bin size). Each bin count was then divided by the total number of network-wide spikes, resulting in probabilities that a spike occurred in the respective bin. For each simulation of a spike time, one of these bins would then be semi-randomly selected according to the respective probabilities determined in the previous step. The precise simulated spike time was then a random time point within the selected bin. This procedure ensured that simulated spike trains followed the general profile of network-wide spiking activity.

For each paired HD-MEA and patch-clamp recording with artificially added ground-truth synaptic input, EPSCs were again estimated with our regression approach. The error between ground-truth EPSC and EPSC estimate was quantified as the mean deviation in percent. Specifically, ground-truth EPSC and EPSC estimate were first normalized by the respective amplitude of the simulated ground-truth EPSC. The mean deviation between these two waveforms within a 30 ms window starting at ground-truth EPSC onset specified the error. The mean error across all experiments (n=14) was eventually calculated for each parameter combination (number of simulated synaptic events and amplitude of simulated EPSC).

The F_1 score was calculated as follows:

$$F_1 = 2 \times \frac{\textit{precision} \times \textit{recall}}{\textit{precision} + \textit{recall}} = \frac{TP}{TP + \frac{1}{2}(FP + FN)} \quad (2)$$

The number of true positives (TP) and false negatives (FN) was the number of accepted and excluded ground-truth connections, respectively (see previous section regarding acceptance criteria). To calculate the number of false positives (FP), we proceeded as follows: we added again artificial units with simulated spike times to all our paired HD-MEA and patch-clamp recordings as before, but this time simulated EPSCs were not added to the patch trace. The artificial unit had therefore no correlated activity in the patch trace. If

the EPSC estimate of this simulated unit was nevertheless accepted by our regression approach, then it was counted as a false positive. The mean F_1 score across all experiments was eventually calculated for each parameter combination.

With increasing EPSC amplitude and increasing number of synaptic events, the error between ground-truth and EPSC estimate quickly became marginal, and the F_1 score reached values near its optimum of 1 (see Fig. 2e in results section). In purely experimental data, the number of synaptic events is dependent on the recording duration and the presynaptic spike rates. Our data set of paired recordings had a mean recording duration of $11.7 \text{ min} \pm 7.0 \text{ min SD}$, which – together with our simulation results – suggested that our approach would only have failed to identify connections with extremely small-amplitude EPSCs and very low presynaptic spike rates.

STA approach for the estimation of synaptic input waveforms

Our alternative approach to estimate synaptic input waveforms, based on paired HD-MEA and patch-clamp recordings, relied on spike-triggered averaging of the patch-clamp current trace using only isolated presynaptic spikes (and the corresponding postsynaptic responses). By 'isolated' we mean presynaptic spike times around which (20 ms before, 10 ms after) none of the other potentially connected units spiked. To obtain a sufficient number of events (≥ 5) for averaging, unconnected units had to be identified and removed first: we iteratively calculated the STA EPSC for each unit (initially tolerating 256/128 spikes in the before/after window and then successively halving the number) and then removed the units that were within the spike tolerance when the absolute EPSC peak amplitude (Amp_E) was smaller than $3 \times \text{s.d.}$ of the pre-spike baseline and smaller than 5 pA. We repeated this procedure until no more units could be removed. Finally, STA EPSCs were calculated using only the isolated events. The remaining units were accepted as being connected to the patched cell when $Amp_E \geq 3 \times \text{s.d.}$ of the baseline and $Amp_E \geq 5 \text{ pA}$.

Reconstruction of synaptic conductance traces

In the main text, we described how the measured whole-cell current trace of the paired patch-clamp and HD-MEA and recording was reconstructed based on the EPSC estimates and corresponding presynaptic unit spike trains by applying the right term of equation 1. We can reconstruct the excitatory and inhibitory synaptic conductances experienced by a postsynaptic cell during the long-term HD-MEA recording of network-wide spiking – which preceded the patch-clamp experiments – in a similar way:

$$g(t) = \frac{1}{dV} \sum_{i \in N_p} \sum_{\tau=0}^{N_\tau} s'_i(t - \tau) w_i(\tau) \quad (3)$$

where $g(t)$ is the synaptic conductance at time point t . As in equation 1, w_i is the EPSC estimate for the i 'th (presynaptic) neuron and N_τ is the number of sample time points of the EPSC estimate; s'_i represents the corresponding (binary) presynaptic spike train. However, as opposed to s_i from equation 1, which is the spike train of presynaptic neuron i from the paired recording, s'_i represents the spike train – of the same neuron i – from the long-term HD-MEA recording period. dV is the driving force (holding potential subtracted by the reversal potential of respective ion channels). N_p specifies the set of presynaptic units that are included in the conductance trace reconstruction. For example, for the g_i and g_e trace reconstructions in Fig. 5, N_p contains all inhibitory or excitatory presynaptic unit IDs, respectively, of a given postsynaptic cell. Similarly, the synaptic conductance of individual monosynaptic connections can be computed (e.g., for Supplementary Fig. 3); in this case, N_p contains only individual presynaptic unit IDs.

Selection of high-conductance events

To calculate the mean conductance trace auto- (ACG) and cross-correlograms (CCG), we selected all high-conductance events that fulfilled the following criteria: both g_e & g_i were continuously for at least $300 \text{ ms} > 2 \times$ s.d. of the respective conductance trace.

To calculate the state-dependent spike-triggered averages of the inhibitory conductance trace, we defined *high g* states to be periods, during which $g_i > 3 \times$ s.d. of g_i trace, following smoothing with a 1k-point Gaussian filter. The remaining recordings period were considered *low g* states.

Spike-transmission probability

The spike-transmission probability (STP) between two cells was always based on the long-term unit spike trains ($> 3 \text{ h}$). For STP estimation, the cross-correlation between the spike trains of the two cells was calculated first (0.5 ms binning). The slow CCG 'baseline' was determined by convolving the CCG with a partially hollow Gaussian kernel (standard deviation=10 ms, hollow fraction=60%), as described before^{33,50}. Subsequently, this baseline was subtracted from the CCG. The baseline-subtracted CCG was then normalized with respect to the number of presynaptic spikes, and the STP estimate was the sum of bins during a certain window of positive lags. When the STP was extracted for the purpose of cell-type classification, a 4 ms window starting at the 1.5 ms positive lag was used. To analyze the relationship between STP and connection strength, the exc/inhEPSC onset latency was used to determine the initial offset of the quantification window. Specifically, to account for differences in the response characteristics, a 4 ms window starting 0.5 ms before excEPSC onset latency was used for excitatory connections, and a 10 ms window starting 1 ms after the inhEPSC onset latency was used for inhibitory connections.

Single-cell level data analysis of incoming connection properties

Several monosynaptic connection properties were determined. The spike rate of the presynaptic unit was the mean of the long-term recording period. The amplitude of the EPSC waveform estimate is the absolute difference between the EPSC peak and the waveform baseline. The EPSC onset latency was defined as the time difference between the time point at which the EPSC waveform reached a value below $-5 \times$ s.d. of the baseline and the presynaptic spike time.

Extracellular unit footprint analysis

To characterize the extracellular electrical unit footprint of a neuron, i.e., the distribution of extracellular electrical potentials across the array electrodes, we generated the spike-triggered average for each of the simultaneously recorded traces (up to 1024; filtered at 0.3–9.5 kHz; spike cutout before/after was 5/10 ms) using the last 1500 spikes of the unit spike train from the long-term HD-MEA recording period. Such a number of spikes was recorded even from the neurons featuring the lowest spike rates. For each average electrode trace, we tested for negative peaks: we detected the first time point (t_0), after spike time, at which the trace reached $< -4 \times$ s.d. of the trace baseline (first 2.5 ms); the peak was then the minimum value between t_0 and t_0+1 ms. Occasionally, especially for some excitatory cells, there were multiple negative peaks in the average electrode trace; possibly because the axonal signal was followed by the extracellular signal of an excited postsynaptic unit, or because the electrode recorded from multiple axonal branches. Our peak detection procedure ensured that only the first extracellular signal peak was used. An electrode trace was excluded if no peak was detected, and if there was no directly adjacent electrode with a detected signal. The signal latency was defined as the time difference between the signal peak of the respective electrode trace and the peak of the electrode trace with the largest (absolute) amplitude within the footprint, which typically was near the axon initial segment (AIS) and soma of the neuron⁵¹.

AP propagation velocity was quantified based on the unit footprint as follows: for each electrode trace, we calculated the AP velocity at the given electrode position using the respective AP signal latency and using the distance – assuming a straight line – between the respective electrode and the cell soma (approximated by the electrode with the largest signal). We used the mean of these individual AP velocity measures to approximate the AP velocity of the neuron. Note that this AP velocity measure will be slightly larger than the true AP velocity, since we assume a straight axonal path between electrode and soma, while the true path will likely deviate from a line. Given this notion, our measure can be interpreted as capturing both AP propagation and how direct the axonal path is.

Statistics

Analyses are based on data from 142 identified connections of 14 patched (excitatory) cells (1 inhibitory cell was excluded) from 5 culture preparations and animals. Statistical analyses were performed in R⁵² and MATLAB (MathWorks). Non-parametric, two-tailed tests were conducted using the Mann-Whitney U test and Wilcoxon signed rank test. Normality was assessed with a Shapiro-Wilk test. Correlations were examined using Pearson's R. The alpha level to determine significance was adjusted for multiple comparisons using the Holm correction when appropriate. No statistical methods were used to predetermine sample sizes. To probe the relationship of connection properties from the perspective of individual postsynaptic cells, we performed linear mixed-effects modeling using the R package *lme4*⁵³. Models contained spike rate and onset latency as fixed effects with random slopes and intercepts, while postsynaptic cell ID was the random effect. A similar analysis was performed to examine the STP - EPSC amplitude relationship. Significance was assessed using a likelihood ratio test³⁴.

Data availability

The data that support the findings of this study are available from the corresponding author upon reasonable request.

Acknowledgements

We would like to thank Vishalini Emmenegger and David Jäckel for their contributions in setting up the rigs for combined HD-MEA and patch-clamp recordings. This work was supported by the ERC Advanced Grant 694829 “neuroXscales”, the Swiss National Science Foundation project 205320-188910, the Swiss National Science Foundation Eccellenza grant PCEFP3_187001 (F.F.), the China Scholarship Council (X.X.), and the ETH Zurich Postdoctoral Fellowship 19-2 FEL-17 (A.P.B).

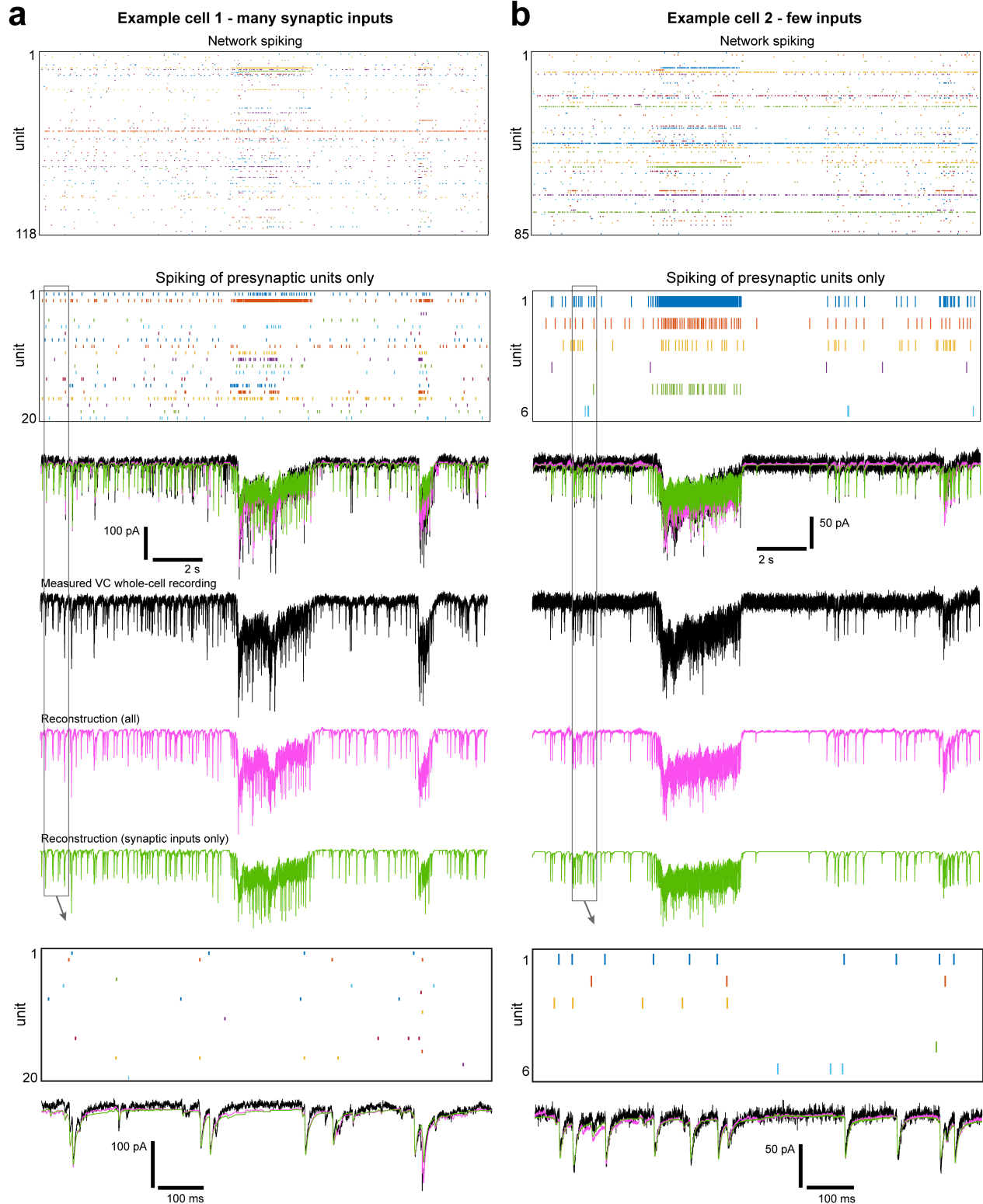
Author contributions

Conceptualization, investigation (unless otherwise stated), analysis (unless otherwise stated), writing of original draft: J.B.; Development of the regression method: F.F.; Intracellular-extracellular-spike analysis: S.S.K.; Confocal-microscopy investigations: A.P.B., X.X., J.B., K.C.K.; Assistance with patch-clamp experiments: T.G.; Spike-sorting support: M.S., T.K.; Supervision and funding acquisition: A.H.; All authors contributed to writing the final version of the manuscript.

Competing interests

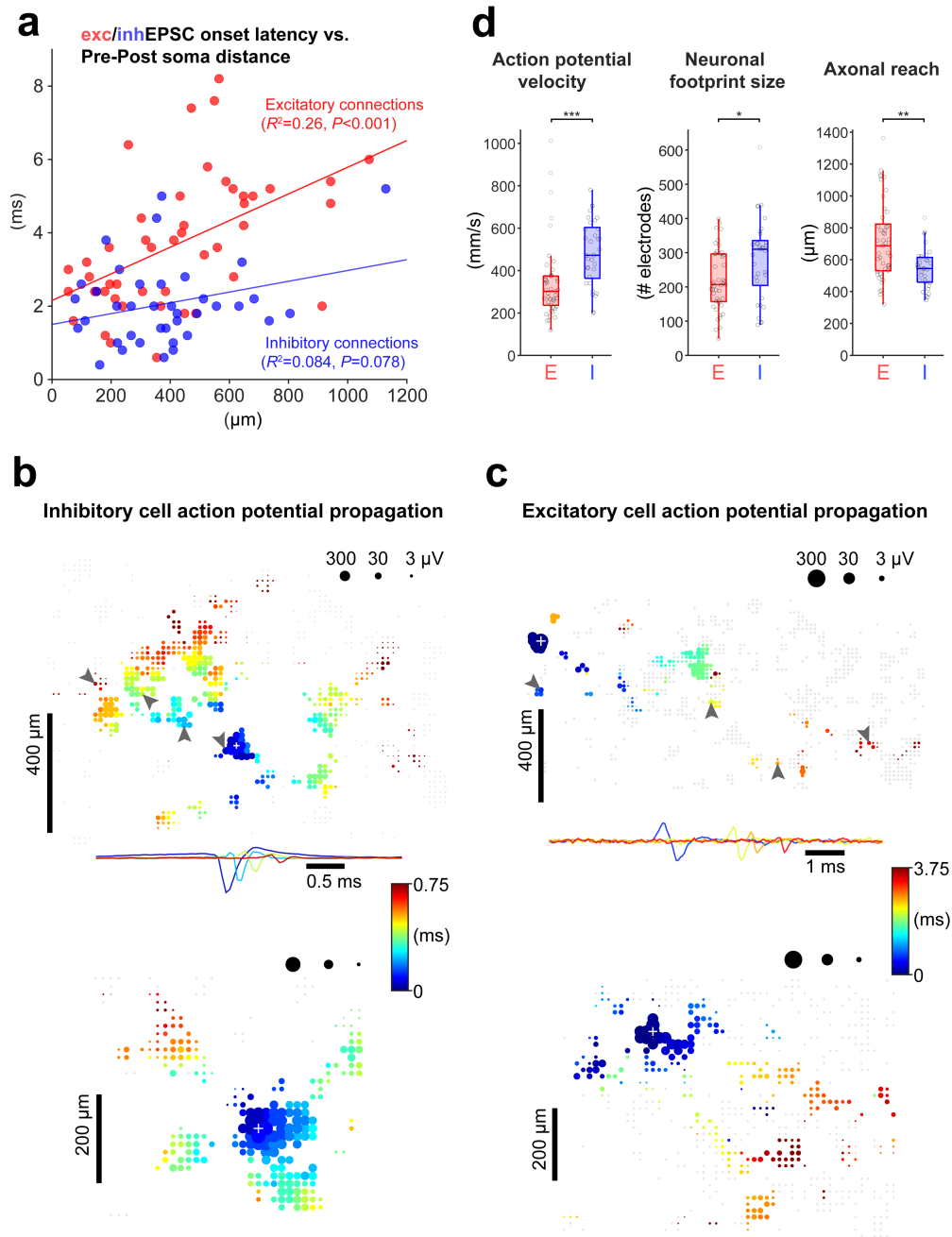
The authors declare no competing interests.

Supplementary Information



Supplementary Figure 1. Variations in the number of identified synaptic inputs

Example synaptic input reconstructions of two neurons that were sequentially patched in the same network and yet displayed a difference in the number of identified incoming connections [(a) 20 vs (b) 6]. Example periods of unit spiking activity of the entire network and only of the respective presynaptic neurons (top two raster plots) are shown, in addition to the measured (black) and reconstructed (magenta/green) input-current traces. The current-trace reconstruction showed a good matching with the measured VC patch-clamp recording for both neurons, which suggests that the difference in identified inputs was of biological origin and not due to an incomplete input mapping.



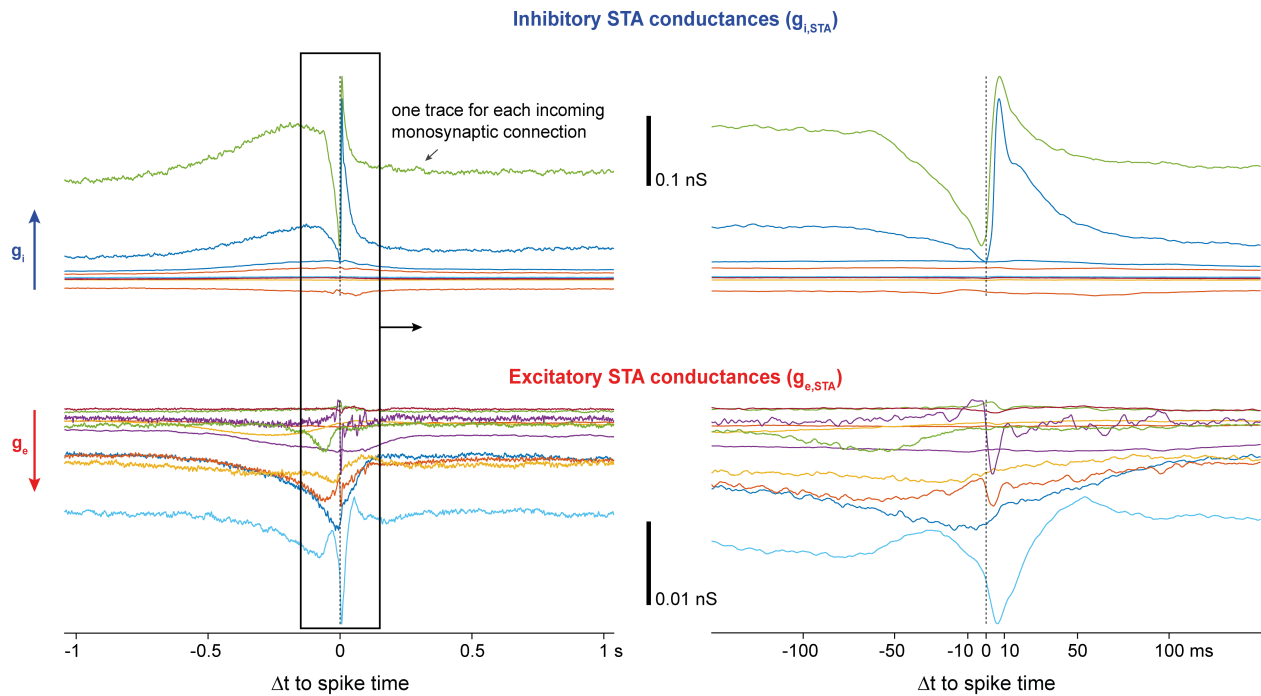
Supplementary Figure 2. Inhibitory and excitatory neurons show differences in action potential propagation, neuronal footprint size and axonal reach

(a) Relationship between excEPSC (red) / inhEPSC (blue) onset latency (relative to presynaptic spike time) and the distance between pre- and postsynaptic cell (the footprint electrode featuring the largest signal, typically near the axon initial segment⁵¹, was the reference point for distance measurements). Lines represent linear regression fits ([E/I] 47/38 connections from 7 cells). (b) To visualize and quantify action potential (AP) propagation for a given unit, the spike-triggered average for all simultaneously recorded traces (up to 1024) was computed, and the peak latency relative to the electrode featuring the largest signal (marked by a white plus sign) was determined. Two example AP latency plots for inhibitory units with an extensive (top) and relatively small (bottom) axonal arbor are shown. Gray arrow heads in the top plot indicate the electrodes for which the STA traces are displayed underneath (filtered at 0.3–9.5 kHz). Gray dots indicate electrodes that did not show any AP signal. White 'gaps' indicate electrodes that were not selected for long-term recording.

(c) As in (b), but for excitatory units.

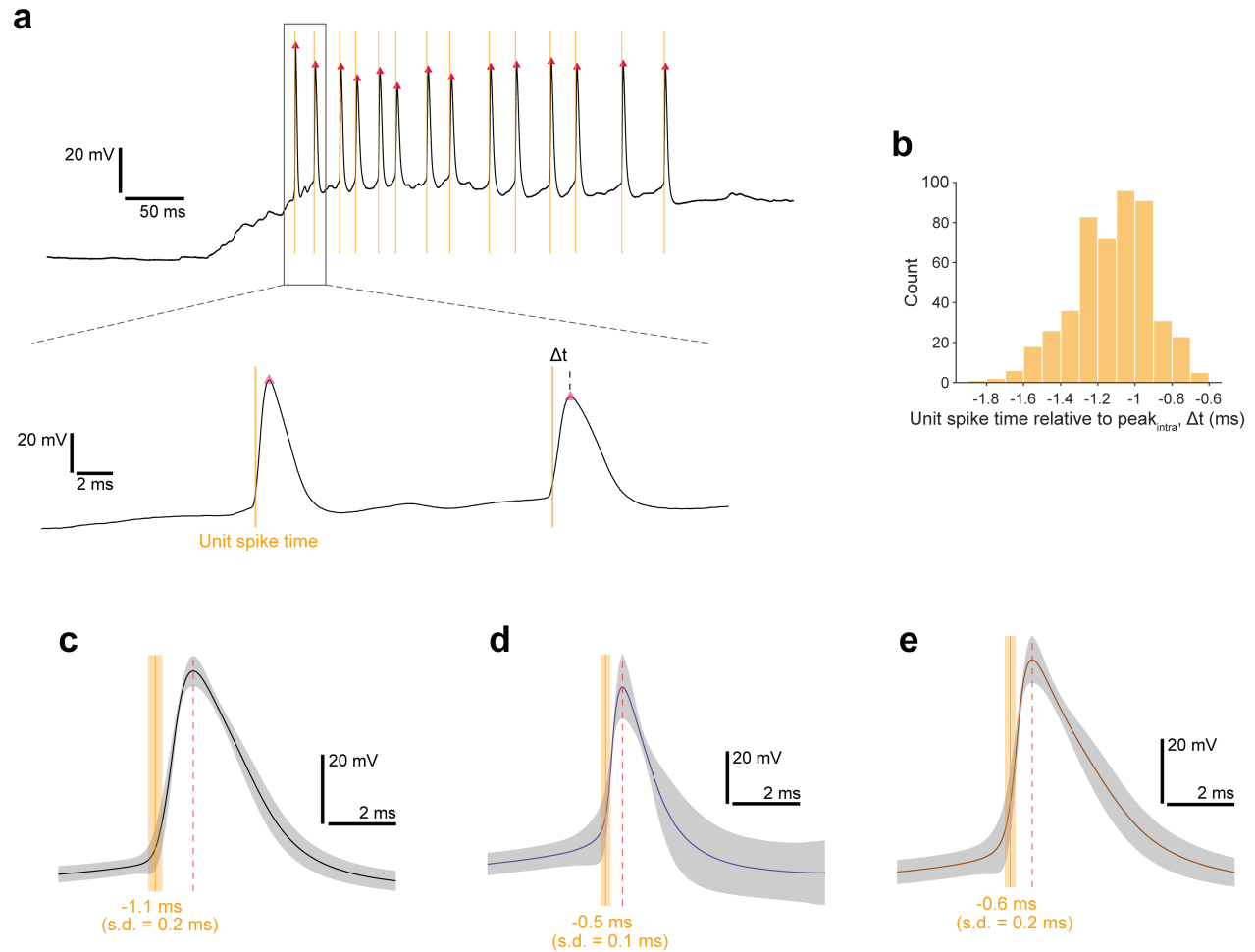
(d) Difference between excitatory and inhibitory units in terms of action potential propagation velocity ($U = 340, P < 0.001$, Mann-Whitney U test), footprint size ($U = 488.5, P = 0.010$) and axonal reach ($U = 425, P = 0.0013$); [E/I] 45/33 pooled presynaptic units; for each unit, 1500 spiking events (# spikes available for all units) were averaged to generate the footprint. AP propagation velocity was quantified based on the AP latencies across the entire unit footprint (see Methods for details). Axonal reach is defined as the 90th percentile of the distances between the electrodes that belong to the unit footprint (i.e., show an AP signature) and the largest signal electrode (presumably near the soma). Box plots indicate median and interquartile ranges, and whiskers the minimum/maximum values except for 36 outliers.

* $P < 0.05$, ** $P < 0.01$, *** $P < 0.001$.



Supplementary Figure 3. Role of individual incoming connections in controlling postsynaptic spiking

The spike-triggered-average conductance, $g_{e/i,STA}$, was calculated separately for the conductance trace of each incoming connection to an example postsynaptic cell (9 inhibitory and 11 excitatory inputs). There appeared to be a few key inputs that had a particularly strong role in controlling postsynaptic spiking. Moreover, there was a subset of excitatory inputs with a sharp increase in conductance near postsynaptic spiking, while others only contributed through slow conductance changes. Interestingly, postsynaptic spiking typically occurred during the early rising phase of the rapid increases in excitatory conductance. As expected, the contribution of each connection to the total STA conductance depended on the respective synaptic strength and presynaptic spike rate: the mean $g_{e/i,STA}$ (from -2 s to +2 s) for each input correlated well with the respective product of input amplitude and presynaptic spike rate, for both excitation ($R^2 = 0.77$; $P < 0.001$; $n = 11$) and inhibition ($R^2 = 0.96$; $P < 0.001$; $n = 9$).



Supplementary Figure 4. Relationship between extracellularly detected unit spike times and corresponding intracellular action potentials

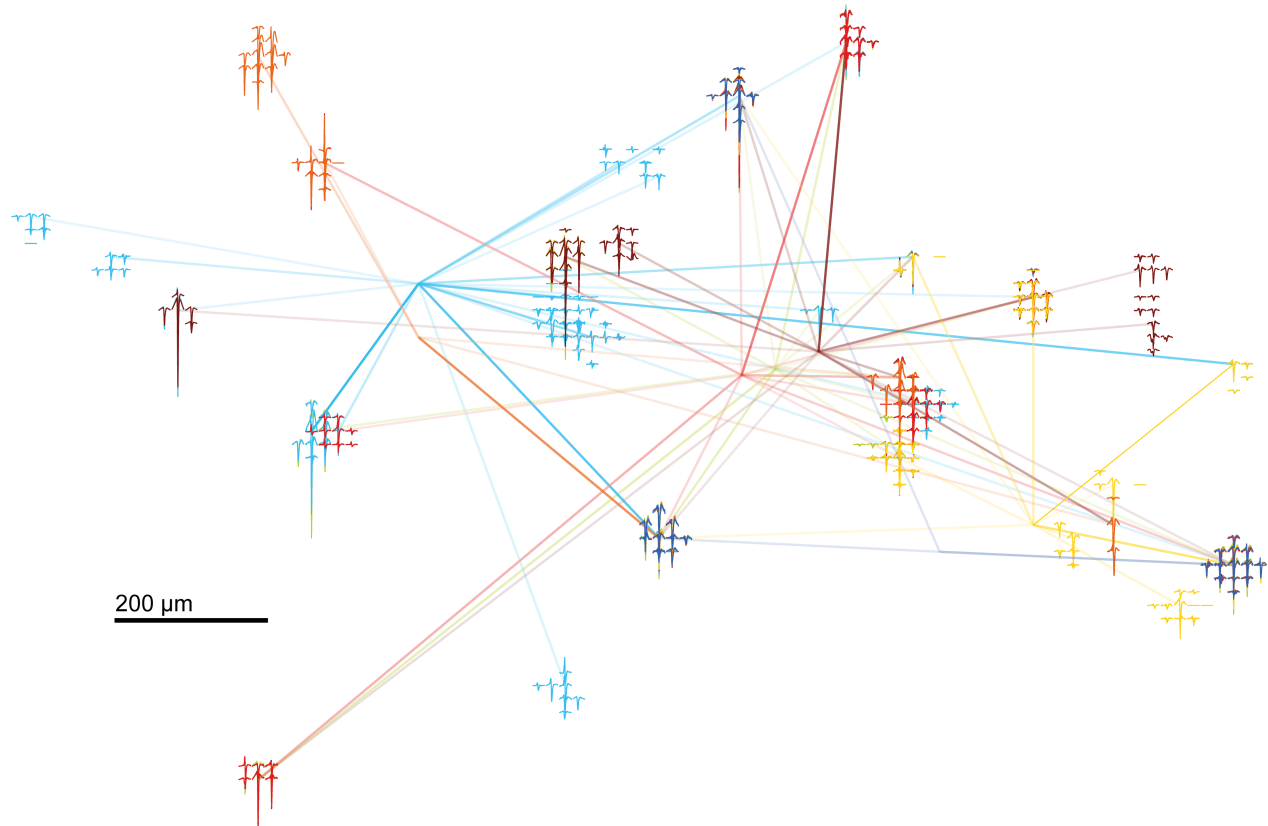
Paired HD-MEA and IC whole-cell patch-clamp recordings during spontaneous spiking activity were performed, and the unit of the patched cell was identified by footprint matching (analogous to Fig. 1e), following spike sorting of the HD-MEA data. An IC internal solution with physiological chloride concentration was used.

(a) Example patch-clamp voltage traces with action potentials. Red triangles mark the peak of the intracellular action potentials. Yellow lines indicate spike times of the unit that corresponded to the patched cell.

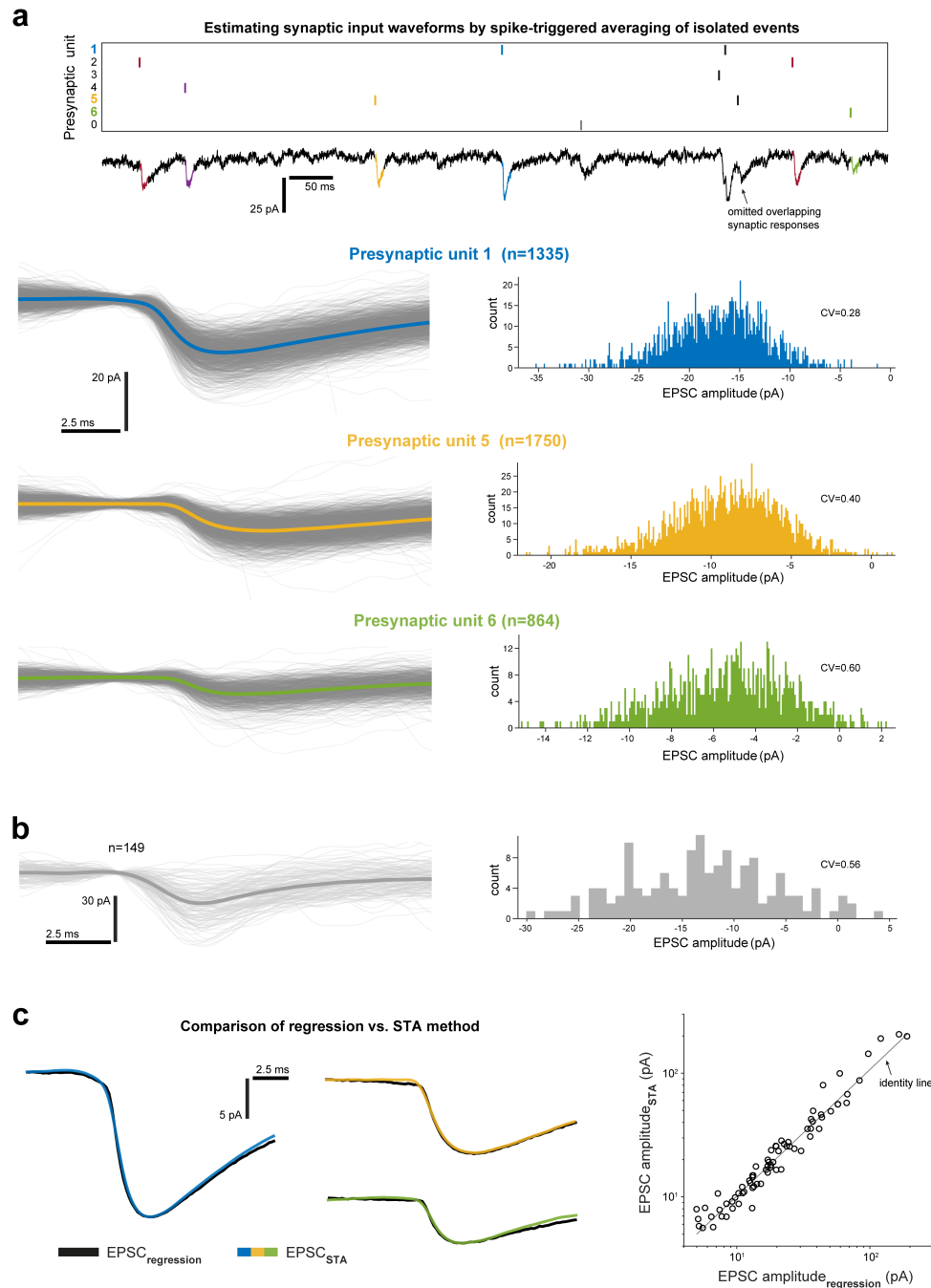
(b) Histogram of the time differences between unit spike time and intracellular action potential peak of the same cell as in (a).

(c) Mean action potential waveform and mean unit spike time (shadings: SD) of the same cell as in (a/b).

(d/e) Results of two more cells, displayed as in (c).



Supplementary Figure 5. Spatial distribution of presynaptic unit footprints and monosynaptic connections that were identified based on multiple paired recordings in the same network. Equivalent to Fig. 8a, with unit footprints shown (filtered at 0.3–9.5 kHz). Only the traces from electrodes near the electrode with the largest signal amplitude are displayed for each unit. Note that some footprints match in terms of both location and signal characteristics, suggesting that the identified units represent the same neuron.



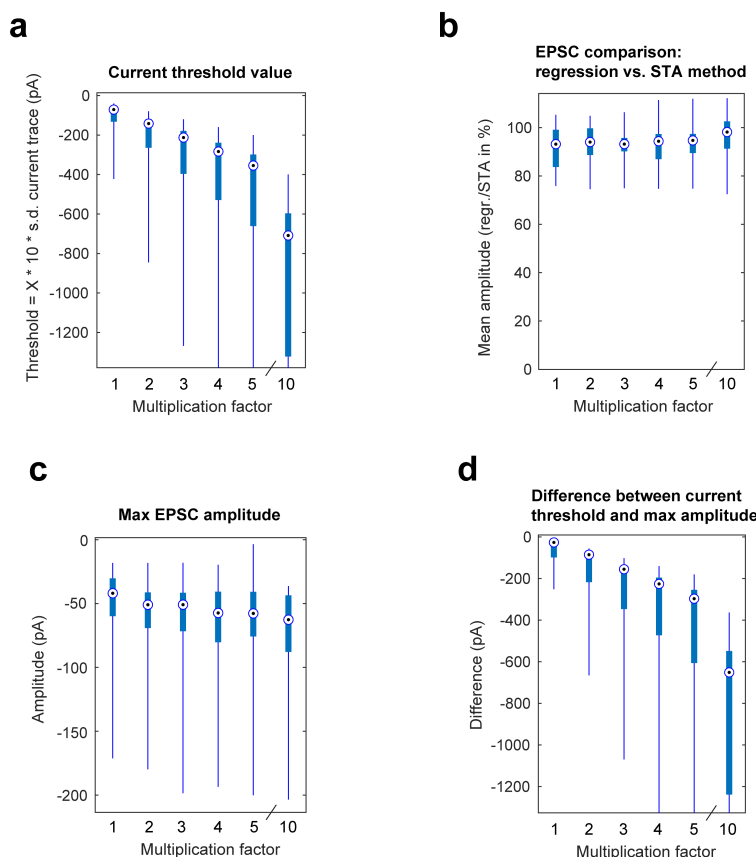
Supplementary Figure 6. Spike-triggered-average-based estimation of EPSC waveforms using paired HD-MEA and patch-clamp recordings

An alternative to the regression-based EPSC estimation approach relied on calculating, for each unit in the network, the spike-triggered average patch response using only ‘isolated events’; that is, presynaptic spike times around which none of the other potentially connected units exhibited spiking (see Methods for details).

(a) Top: example spike raster plot of presynaptic activity with corresponding whole-cell current-clamp recording. Isolated events are highlighted in colour. Overlapping responses (arrow) were excluded. (‘Unit 0’ contains spike times from units that might be connected to the patched cell, but without reasonable confidence). Bottom: for three example inputs, the mean (colored) and the individual EPSCs (gray) across the entire recording are shown, in addition to the respective EPSC amplitude histogram (a Gaussian filter with a 20-element sliding window was applied to individual response traces for better visualization; mean trace based on raw data).

(b) Another example of evoked EPSCs and amplitude histogram from a separate recording. ‘Peaks’ in the amplitude distribution consistent with multi-site quantal release.

(c) Left: Comparison of EPSC-waveform estimates based on regression vs. STA method of example connections shown in (a). Right: EPSC amplitudes, based on connections identified by both methods, were highly correlated.



Supplementary Figure 7. Effect of inclusion current thresholds on the estimation of EPSC waveforms

Different current thresholds, that determined which parts of the recording were included in the regression analysis, were applied to the patch-clamp current traces. The threshold values were multiples of the standard deviation of the respective current trace. Specifically, for each recording, 6 threshold values were evaluated: 1, 2, 3, 4, 5 & $10 \times \text{s.d.}$ of the current trace.

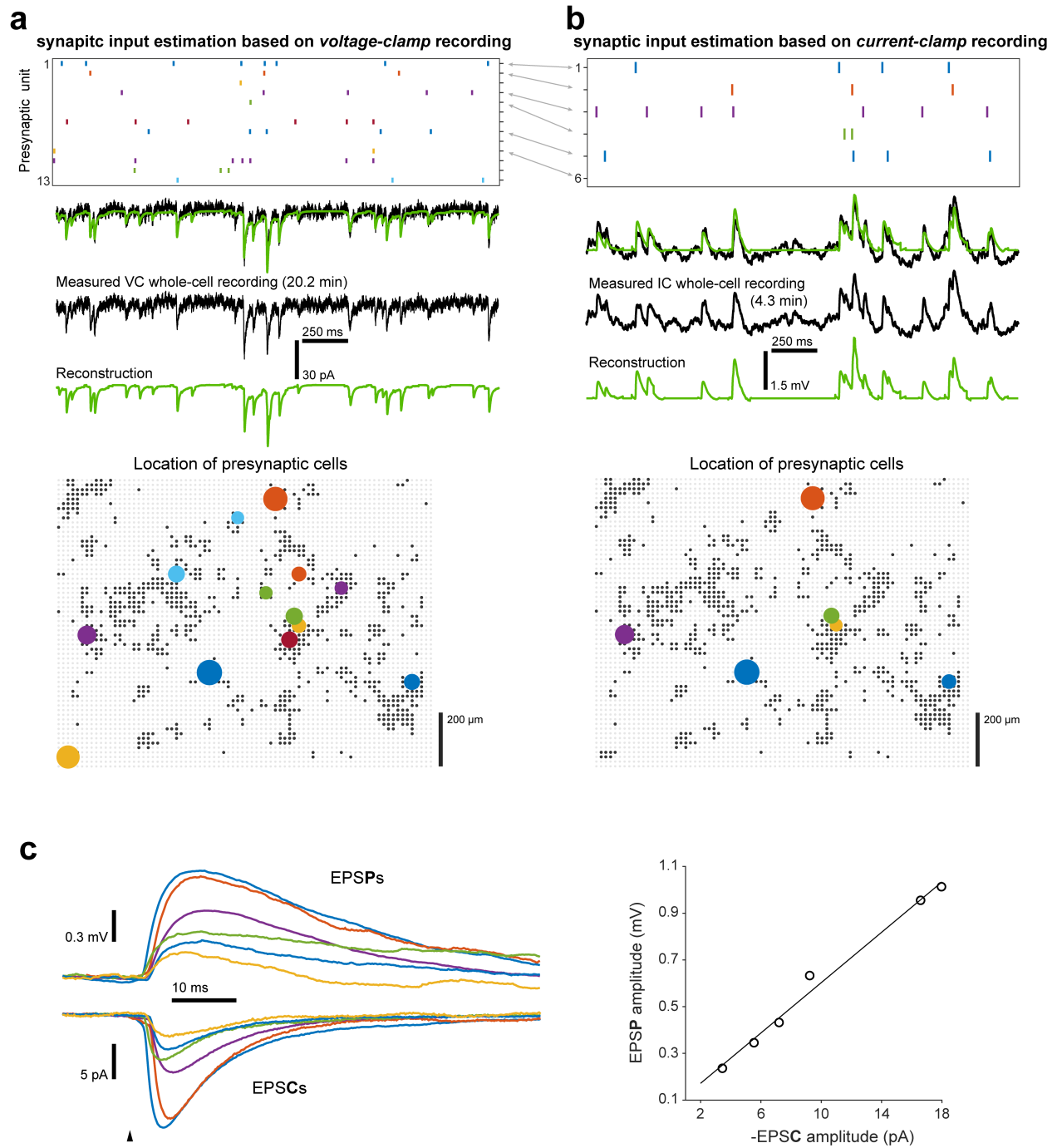
(a) The determined current thresholds across experiments.

(b) We used the EPSCs determined by our STA method, which was performed without any inclusion criteria involving current thresholds, as ground-truth EPSCs. To these ground-truth EPSCs we compared the regression-EPSC estimates that were determined using the different current thresholds. Specifically, for each paired recording, we calculated for each common synaptic input the ratio of the EPSC amplitudes determined by the regression and STA method. The mean of these ratios was calculated for each postsynaptic cell, which is summarized here.

(c) Largest EPSC amplitude for each cell.

(d) Difference between current threshold and largest EPSC amplitude. In all panels, box plots indicate median and interquartile ranges, and whiskers the minimum/maximum values (no outliers). Some extreme whiskers in (a) and (d) were trimmed for better data visibility. [14 cells in (a-d); 9 patched cells in (b), where recordings were only included if at least three common inputs were identified by using the two methods.]

Compared to the EPSC amplitudes determined by the STA method, the different current thresholds had only a small effect on the EPSC amplitudes that were determined by the regression-based method (b). Moreover, the maximum EPSC amplitude that was identified showed little dependence on the current threshold (c). These findings suggested that synaptic inputs exhibited sufficient activity – i.e., for a reliable EPSC estimation – during periods that were selected by even the smallest current thresholds. Moreover, the current threshold values were well above the maximum EPSC amplitudes as confirmed in (d). We chose a threshold of $30 \times \text{s.d.}$ of the current trace, which resulted in a median current threshold of approximately 200 pA, with sufficient distance to the maximum EPSC amplitude, while also keeping computational costs within a feasible range.



Supplementary Figure 8. Estimation of synaptic input waveforms based on current-clamp recordings

Two paired HD-MEA and whole-cell patch-clamp recordings were acquired from the same cell in either voltage-clamp (**a**) or current-clamp mode (**b**).

(**a/b**) Top: raster plot of the identified presynaptic units of an example period (corresponding presynaptic cells are marked by grey arrows). Middle: patch-clamp recording (black) and reconstruction based on synaptic inputs (green). Bottom: location of presynaptic cells; one coloured filled circle per cell (black dots: HD-MEA electrodes selected for recording; grey dots: electrodes not recorded from). The same presynaptic cells identified in (**a**) and (**b**) have matching colours. The larger the circle the stronger the connection.

(**c**) Left: Corresponding EPSP- and EPSC-waveform estimates (waveforms from the same input have matching colors). Right: Correlation of EPSP and EPSC amplitudes (linear regression fit; $R^2 = 0.99$).

References

- ¹ Steriade, M., Timofeev, I. & Grenier, F. Natural waking and sleep states: a view from inside neocortical neurons. *Journal of neurophysiology* **85**, 1969–1985 (2001).
- ² Timofeev, I., Grenier, F. & Steriade, M. Disfacilitation and active inhibition in the neocortex during the natural sleep-wake cycle: an intracellular study. *Proceedings of the National Academy of Sciences* **98**, 1924–1929 (2001).
- ³ Destexhe, A., Rudolph, M. & Paré, D. The high-conductance state of neocortical neurons in vivo. *Nature reviews neuroscience* **4**, 739–751 (2003).
- ⁴ Steriade, M., Nunez, A. & Amzica, F. A novel slow (< 1 hz) oscillation of neocortical neurons in vivo: depolarizing and hyperpolarizing components. *Journal of neuroscience* **13**, 3252–3265 (1993).
- ⁵ Sanchez-Vives, M. V. & McCormick, D. A. Cellular and network mechanisms of rhythmic recurrent activity in neocortex. *Nature neuroscience* **3**, 1027–1034 (2000).
- ⁶ Shu, Y., Hasenstaub, A. & McCormick, D. A. Turning on and off recurrent balanced cortical activity. *Nature* **423**, 288–293 (2003).
- ⁷ Haider, B. & McCormick, D. A. Rapid neocortical dynamics: cellular and network mechanisms. *Neuron* **62**, 171–189 (2009).
- ⁸ Liu, G. Local structural balance and functional interaction of excitatory and inhibitory synapses in hippocampal dendrites. *Nature neuroscience* **7**, 373–379 (2004).
- ⁹ Van Pelt, J., Corner, M., Wolters, P., Rutten, W. & Ramakers, G. Longterm stability and developmental changes in spontaneous network burst firing patterns in dissociated rat cerebral cortex cell cultures on multielectrode arrays. *Neuroscience letters* **361**, 86–89 (2004).
- ¹⁰ Wagenaar, D. A., Pine, J. & Potter, S. M. An extremely rich repertoire of bursting patterns during the development of cortical cultures. *BMC neuroscience* **7**, 1–18 (2006).
- ¹¹ Wagenaar, D. A., Nadasdy, Z. & Potter, S. M. Persistent dynamic attractors in activity patterns of cultured neuronal networks. *Physical Review E* **73**, 051907 (2006).
- ¹² Bartram, J. *et al.* Cortical up states induce the selective weakening of subthreshold synaptic inputs. *Nature communications* **8**, 1–11 (2017).

- ¹³ Pan, Y. & Monje, M. Activity shapes neural circuit form and function: a historical perspective. *Journal of Neuroscience* **40**, 944–954 (2020).
- ¹⁴ Seamans, J. K., Nogueira, L. & Lavin, A. Synaptic basis of persistent activity in prefrontal cortex in vivo and in organotypic cultures. *Cerebral Cortex* **13**, 1242–1250 (2003).
- ¹⁵ Isaacson, J. S. & Scanziani, M. How inhibition shapes cortical activity. *Neuron* **72**, 231–243 (2011).
- ¹⁶ Ahmadian, Y. & Miller, K. D. What is the dynamical regime of cerebral cortex? *Neuron* **109**, 3373–3391 (2021).
- ¹⁷ Brunel, N. Dynamics of sparsely connected networks of excitatory and inhibitory spiking neurons. *Journal of computational neuroscience* **8**, 183–208 (2000).
- ¹⁸ Amit, D. J. & Brunel, N. Model of global spontaneous activity and local structured activity during delay periods in the cerebral cortex. *Cerebral cortex (New York, NY: 1991)* **7**, 237–252 (1997).
- ¹⁹ Van Vreeswijk, C. & Sompolinsky, H. Chaos in neuronal networks with balanced excitatory and inhibitory activity. *Science* **274**, 1724–1726 (1996).
- ²⁰ Destexhe, A., Rudolph, M., Fellous, J.-M. & Sejnowski, T. J. Fluctuating synaptic conductances recreate in vivo-like activity in neocortical neurons. *Neuroscience* **107**, 13–24 (2001).
- ²¹ Hasenstaub, A. *et al.* Inhibitory postsynaptic potentials carry synchronized frequency information in active cortical networks. *Neuron* **47**, 423–435 (2005).
- ²² Buzsáki, G. & Wang, X.-J. Mechanisms of gamma oscillations. *Annual review of neuroscience* **35**, 203–225 (2012).
- ²³ Renart, A., Moreno-Bote, R., Wang, X.-J. & Parga, N. Mean-driven and fluctuation-driven persistent activity in recurrent networks. *Neural computation* **19**, 1–46 (2007).
- ²⁴ Petersen, P. C. & Berg, R. W. Lognormal firing rate distribution reveals prominent fluctuation-driven regime in spinal motor networks. *Elife* **5**, e18805 (2016).
- ²⁵ Okun, M. & Lampl, I. Instantaneous correlation of excitation and inhibition during ongoing and sensory-evoked activities. *Nature neuroscience* **11**, 535–537 (2008).
- ²⁶ Atallah, B. V. & Scanziani, M. Instantaneous modulation of gamma oscillation frequency by balancing excitation with inhibition. *Neuron* **62**, 566–577 (2009).

- ²⁷ Piwkowska, Z. *et al.* Characterizing synaptic conductance fluctuations in cortical neurons and their influence on spike generation. *Journal of neuroscience methods* **169**, 302–322 (2008).
- ²⁸ Barral, J. & Reyes, A. D. Synaptic scaling rule preserves excitatory–inhibitory balance and salient neuronal network dynamics. *Nature neuroscience* **19**, 1690–1696 (2016).
- ²⁹ Pillow, J. W., Shlens, J., Chichilnisky, E. & Simoncelli, E. P. A model-based spike sorting algorithm for removing correlation artifacts in multi-neuron recordings. *PloS one* **8**, e62123 (2013).
- ³⁰ Barthó, P. *et al.* Characterization of neocortical principal cells and interneurons by network interactions and extracellular features. *Journal of neurophysiology* **92**, 600–608 (2004).
- ³¹ Campagnola, L. *et al.* Local connectivity and synaptic dynamics in mouse and human neocortex. *bioRxiv* (2021).
- ³² Mizuseki, K. & Buzsáki, G. Preconfigured, skewed distribution of firing rates in the hippocampus and entorhinal cortex. *Cell reports* **4**, 1010–1021 (2013).
- ³³ English, D. F. *et al.* Pyramidal cell-interneuron circuit architecture and dynamics in hippocampal networks. *Neuron* **96**, 505–520 (2017).
- ³⁴ Yu, Z. *et al.* Beyond t test and anova: applications of mixed-effects models for more rigorous statistical analysis in neuroscience research. *Neuron* (2021).
- ³⁵ Rudolph, M., Pospischil, M., Timofeev, I. & Destexhe, A. Inhibition determines membrane potential dynamics and controls action potential generation in awake and sleeping cat cortex. *Journal of neuroscience* **27**, 5280–5290 (2007).
- ³⁶ Salkoff, D. B., Zaghera, E., Yüzgeç, Ö. & McCormick, D. A. Synaptic mechanisms of tight spike synchrony at gamma frequency in cerebral cortex. *Journal of Neuroscience* **35**, 10236–10251 (2015).
- ³⁷ Cutts, C. S. & Eglén, S. J. Detecting pairwise correlations in spike trains: an objective comparison of methods and application to the study of retinal waves. *Journal of Neuroscience* **34**, 14288–14303 (2014).
- ³⁸ Barbour, B., Brunel, N., Hakim, V. & Nadal, J.-P. What can we learn from synaptic weight distributions? *TRENDS in Neurosciences* **30**, 622–629 (2007).
- ³⁹ Buzsáki, G. & Mizuseki, K. The log-dynamic brain: how skewed distributions affect network operations. *Nature Reviews Neuroscience* **15**, 264–278 (2014).

- ⁴⁰ Peng, Y. *et al.* High-throughput microcircuit analysis of individual human brains through next-generation multineuron patch-clamp. *Elife* **8**, e48178 (2019).
- ⁴¹ Wehr, M. & Zador, A. M. Balanced inhibition underlies tuning and sharpens spike timing in auditory cortex. *Nature* **426**, 442–446 (2003).
- ⁴² Monier, C., Chavane, F., Baudot, P., Graham, L. J. & Frégnac, Y. Orientation and direction selectivity of synaptic inputs in visual cortical neurons: a diversity of combinations produces spike tuning. *Neuron* **37**, 663–680 (2003).
- ⁴³ Bonifazi, P. *et al.* Gabaergic hub neurons orchestrate synchrony in developing hippocampal networks. *Science* **326**, 1419–1424 (2009).
- ⁴⁴ Cossart, R. Operational hub cells: a morpho-physiologically diverse class of gabaergic neurons united by a common function. *Current opinion in neurobiology* **26**, 51–56 (2014).
- ⁴⁵ Gal, E. *et al.* The role of hub neurons in modulating cortical dynamics. *Frontiers in neural circuits* 96 (2021).
- ⁴⁶ Müller, J. *et al.* High-resolution cmos mea platform to study neurons at subcellular, cellular, and network levels. *Lab on a Chip* **15**, 2767–2780 (2015).
- ⁴⁷ Csicsvari, J., Hirase, H., Czurko, A. & Buzsáki, G. Reliability and state dependence of pyramidal cell–interneuron synapses in the hippocampus: an ensemble approach in the behaving rat. *Neuron* **21**, 179–189 (1998).
- ⁴⁸ Senzai, Y. & Buzsáki, G. Physiological properties and behavioral correlates of hippocampal granule cells and mossy cells. *Neuron* **93**, 691–704 (2017).
- ⁴⁹ Weir, K., Blanquie, O., Kilb, W., Luhmann, H. J. & Sinning, A. Comparison of spike parameters from optically identified gabaergic and glutamatergic neurons in sparse cortical cultures. *Frontiers in cellular neuroscience* **8**, 460 (2015).
- ⁵⁰ Stark, E. & Abeles, M. Unbiased estimation of precise temporal correlations between spike trains. *Journal of neuroscience methods* **179**, 90–100 (2009).
- ⁵¹ Bakkum, D. J. *et al.* The axon initial segment is the dominant contributor to the neuron’s extracellular electrical potential landscape. *Advanced biosystems* **3**, 1800308 (2019).
- ⁵² R Core Team. *R: A Language and Environment for Statistical Computing*. R Foundation for Statistical Computing, Vienna, Austria (2021). URL <https://www.R-project.org/>.

⁵³ Bates, D., Mächler, M., Bolker, B. & Walker, S. Fitting linear mixed-effects models using lme4. *Journal of Statistical Software* **67**, 1–48 (2015). URL <https://www.jstatsoft.org/index.php/jss/article/view/v067i01>.